Elsevier Editorial System(tm) for Icarus
Manuscript Draft

Manuscript Number:

Title: Optimal dynamos in the cores of terrestrial exoplanets: Magnetic field generation and detectability

Article Type: Regular Article

Keywords: Extrasolar planets
Geophysics
Interiors
Magnetic fields
Radio observations

Corresponding Author: Dr. Peter E Driscoll, PhD

Corresponding Author's Institution: Johns Hopkins University

First Author: Peter E Driscoll, PhD

Order of Authors: Peter E Driscoll, PhD; Peter L Olson, PhD

Abstract: A promising way to gain knowledge about the internal dynamics of extrasolar planets is by remote measurement of an intrinsic magnetic field. A magnetic field is helpful for shielding the upper atmosphere from stellar wind induced mass loss and retaining water over long (Gyr) time scales. Strong planetary magnetic fields are maintained by internal dynamo action in an electrically conducting fluid layer. Here we present a whole planet dynamo model that consists of three main components: an internal structure model with composition and layers similar to the Earth, an optimal mantle convection model that is designed to maximize the core heat flow available to drive convective dynamo action in the core, and a scaling law to estimate the magnetic field intensity at the planetary surface of a terrestrial exoplanet. No internal heat sources are included in the mantle so that the upper mantle thermal boundary layer heat flow is equal to that in the lower mantle, and is fundamentally limited by the silicate solidus and the critical Rayleigh number for the onset of convection. In this limit we find total core heat flows of 40-200 TW, with an adiabatic core heat flow of about 30% of the total on average, for 1-10 Earth-mass exoplanets. In otherwise similar models with larger cores (65% mass fraction) the total core heat flow is about 10% lower, with an adiabatic core heat flow of about 50% of the total. We find that the magnetic field intensity at the core surface for all models is about twice the present-day geomagnetic field intensity there, and the magnetic moment varies by a factor of 20 over the models considered. Assuming electron cyclotron emission is produced from the interaction between the stellar wind and the exoplanet magnetic field we estimate the emission flux and frequency for nearby super-Earth exoplanets. In general we find cyclotron frequencies less than the ionospheric cutoff at 10 MHz and emission fluxes in the range 10^-4 to 10^-7 Jy, well below the current detection threshold of the largest radio telescopes. However, we propose anomalous boosts and modulations of the cyclotron emission that may allow for their detection in the future.

Suggested Reviewers: Christophe Sotin PhD
Researcher, Jet Propulsion Laboratory, NASA

christophe.sotin@univ-nantes.fr

Stephan Labrosse PhD
Professor, Laboratoire des sciences de la Terre, ENS Lyon
stephane.labrosse@ens-lyon.fr

Francis Nimmo PhD
Professor, Earth and Planetary Sciences, University of California Santa Cruz
fnimmo@es.ucsc.edu

Lars Stixrude PhD
Professor, Earth Sciences, University College London
l.stixrude@ucl.ac.uk

Opposed Reviewers: Clint Conrad PhD
Professor, University of Hawaii
Dr. Conrad recently submitted a paper on extrasolar magnetic fields to another journal so he may have conflicting interests.

Eric Gaidos PhD
University of Hawaii
Conflicting interest.

Michael Manga PhD
University of California Berkeley
Conflicting interest.

John Hernlund PhD
University of California Berkeley
Conflicting interest.

Cover Letter

JOHNS HOPKINS
UNIVERSITY

The Morton K. Blaustein
Department of Earth and Planetary Sciences
301 Olin Hall / 3400 N. Charles Street
Baltimore MD 21218-2681
410-516-7135 / Fax 410-516-7933

April 29, 2010

Dear Editor:

I am pleased to submit our paper entitled “Optimal dynamos in the cores of terrestrial exoplanets: Magnetic field generation and detectability” for publication in ***ICARUS.***

In this paper we explore the optimal conditions for dynamo action in the cores of terrestrial exoplanets by constructing a whole planet internal structure and thermal profile assuming mobile lid, sub-solidus mantle convection. We relate the thermal buoyancy flux in the core to magnetic field intensity using a dynamo scaling law and show that planets with large cores can sustain strong magnetic fields. We estimate the cyclotron emission frequency from exoplanet magnetic fields and assess the possibility of detection with radio telescopes. Measurement of magnetic fields in terrestrial extrasolar planets provides unique insight into their internal dynamics, and may have important implications for surface tectonics and atmospheric shielding.

ICARUS has become a valuable resource for exoplanet studies and this is why we have chosen to bring this paper to your attention. We look forward to receiving your and the referees’ evaluations.

Sincerely,

Peter Driscoll and Peter Olson
Johns Hopkins University
Baltimore, MD USA
(peter.driscoll@jhu.edu)

Optimal dynamos in the cores of terrestrial exoplanets: Magnetic field generation and detectability

Peter Driscoll and Peter Olson

Earth & Planetary Sciences, Johns Hopkins University, MD 21218

In preparation for *ICARUS*

Abstract

A promising way to gain knowledge about the internal dynamics of extrasolar planets is by remote measurement of an intrinsic magnetic field. A magnetic field is helpful for shielding the upper atmosphere from stellar wind induced mass loss and retaining water over long (Gyr) time scales. Strong planetary magnetic fields are maintained by internal dynamo action in an electrically conducting fluid layer. Here we present a whole planet dynamo model that consists of three main components: an internal structure model with composition and layers similar to the Earth, an optimal mantle convection model that is designed to maximize the core heat flow available to drive convective dynamo action in the core, and a scaling law to estimate the magnetic field intensity at the planetary surface of a terrestrial exoplanet. No internal heat sources are included in the mantle so that the upper mantle thermal boundary layer heat flow is equal to that in the lower mantle, and is fundamentally limited by the silicate solidus and the critical Rayleigh number for the onset of convection. In this limit we find total core heat flows of 40-200 TW, with an adiabatic core heat flow of about 30% of the total on average, for 1-10 Earth-mass exoplanets.

In otherwise similar models with larger cores (65% mass fraction) the total core heat flow is about 10% lower, with an adiabatic core heat flow of about 50% of the total. We find that the magnetic field intensity at the core surface for all models is about twice the present-day geomagnetic field intensity there, and the magnetic moment varies by a factor of 20 over the models considered. Assuming electron cyclotron emission is produced from the interaction between the stellar wind and the exoplanet magnetic field we estimate the emission flux and frequency for nearby super-Earth exoplanets. In general we find cyclotron frequencies less than the ionospheric cutoff at 10 MHz and emission fluxes in the range $10^{-4} - 10^{-7}$ Jy, well below the current detection threshold of the largest radio telescopes. However, we propose anomalous boosts and modulations of the cyclotron emission that may allow for their detection in the future.

Key words: Extrasolar planets, Geophysics, Interiors, Magnetic fields, Radio observations

1 Introduction

Planetary magnetic fields maintained by internal dynamo action are present, or have existed in the past, within every planet in the solar system with the possible exception of Venus. Detection of a terrestrial exoplanet dynamo provides important constraints on the internal structure, dynamics, and possibly surface tectonics. Mobile-lid mantle convection is favorable for efficient heat transfer from the deep interior so that planets with strong magnetic fields may imply vigorously convecting mantles and active surface tectonics. Furthermore, the need to retain large amounts of water to maintain a habitable surface over long time-scales may require a magnetic field to shield the atmosphere from mass loss and the surface from charged particles (Dehant et al., 2007; Lammer et al., 2007; Kasting, 1995). Therefore,

Email address: peter.driscoll@jhu.edu, Phone: 410-516-7707 (Peter Driscoll).

the search for terrestrial exoplanet magnetic fields is a critical component of the search for habitable planets.

Without a large scale planetary magnetic field, charged particles interact with the upper atmosphere and accelerate non-thermal escape and atmospheric mass loss. More frequent solar flares and increased solar wind flux associated with the active young Sun amplify these effects during the early stages of planetary evolution. Earth's strong magnetic field shields its atmosphere from these escape processes, fostering the retention of large amounts of water in the surface environment. This may not have been the case for the other terrestrial planets. For example the measured D/H ratio in the Venusian atmosphere indicates that it had more water in the past (Lammer et al., 2008), consistent with the absence of a strong magnetic field.

Maintenance of a convective dynamo in a large terrestrial planet is controlled by the rate of heat transfer from the deep interior, which is enhanced by the presence of large scale mantle convection and mobile-lid surface tectonics (Nimmo and Stevenson, 2000). Both Venus and Mars likely had some form of active surface tectonics in the past, which may have ceased in conjunction with the loss of water from their surfaces. Extinction of dynamo action in the core may be related to these events (Nimmo, 2002; Stevenson, 2001).

The detection of extrasolar planetary magnetic fields offers unique insight to the internal structure and dynamics of these planets (Stevenson, 2003). More than 400 extrasolar planets have been detected to date, with 20 planets less massive than 10 M_E (M_E = 1 Earth mass) (Schneider, 2010). Although the diversity among extrasolar planets has been surprising (Fischer, 2008; Butler et al., 2006), the key ingredients to sustaining a dynamo, an energy source (i.e. convection), rotation, and a large volume of electrically conducting fluid, are thought to be common planetary phenomenon. Numerical simulations indicate that planets in the 1-10 Earth-mass regime with an Earth-like (terrestrial) composition that harbor large, mostly iron cores form readily within 3 AU of their host star (Laughlin et al., 2004; Ida and Lin, 2004), and are often referred to as "super-Earths" (Seager et al., 2007; Valencia et al.,

2006). In this paper we explore the optimal thermal state of a terrestrial exoplanet that maximizes the magnetic field strength of the core dynamo.

The magnetic planets in the Solar System emit intense electron cyclotron radiation at radio frequencies (1-100 MHz), which is generated by energetic solar wind electrons interacting with the planetary magnetic field. Cyclotron emission is modulated at the rotation period of the planet if the magnetic field contains non-axisymmetric components and has been used to estimate the rotation periods of the giant planets (e.g. Anderson and Schubert, 2007; Zarka et al., 2001). Extrasolar planets with strong magnetic fields are expected to produce detectable cyclotron emission at radio frequencies (Zarka, 2007). Several other techniques have been proposed to detect and measure the magnetic fields of extrasolar planets and evidence of interaction between the magnetic field of a star and exoplanet has been claimed in about 10 cases (e.g. Shkolnik et al., 2003, 2008). We aim here to explore the detectability of low mass, terrestrial-type exoplanet magnetic fields.

Models of the radial variation of density in planets with end member compositions were first constructed in the pioneering work of Zapolsky and Salpeter (1969). Recently, various preliminary internal structure models of super-Earths have been constructed to obtain simple scaling laws for the planetary and core radius as a function of planetary mass (e.g. Valencia et al., 2006; Seager et al., 2007; Sotin et al., 2007). These models either ignore the thermal state of the mantle and core and phase transitions therein or assume a core-mantle boundary (CMB) heat flux proportional to planet mass. In this study we compute internal structure models with self-consistent thermal convection profiles that are optimal for dynamo action in the core. Our internal structure and temperature profiles are used to calculate the core heat flow, core conductivity, and other properties, which are used to estimate the magnetic field intensity from a dynamo scaling law.

Before introducing the specifics of the model it is helpful to list the main assumptions and idealizations of the optimal model. They are: an Earth-like composition and structure, surface temperature $T_0 = 300$ K and pressure $P_0 = 1$ atm, no secular cooling or internal

heating in the mantle, and a fast (Earth-like) rotation rate.

We describe the internal structure model in §2, the optimal thermal model in §3, and the magnetic field scaling law in §4. The main results are presented in §5, and considerations of magnetic field detectability are in §6. We discuss the thermal state of the terrestrial planets in the solar system in §7. Finally, we summarize our main conclusions and discuss the prospects for detecting an exoplanet magnetic field in the near future in §8.

2 Internal structure model

The internal structure modeling technique employed here is very similar to those of Valencia et al. (2006), Sotin et al. (2007), and Seager et al. (2007). The following set of equations are solved in a spherical shell of thickness dr and are then integrated over the full radius of the planet R subject to boundary conditions. The continuity equation describing the change in mass $m(r)$ within radius r, Poisson's equation for gravity g, the hydrostatic equation for pressure P, and the Adams-Williamson equation for density ρ are,

$$dm(r)/dr = 4\pi r^2 \rho(r) \tag{1}$$
$$dg(r)/dr = 4\pi G\rho(r) - 2Gm(r)/r^3 \tag{2}$$
$$dP(r)/dr = -\rho(r)g(r) \tag{3}$$
$$d\rho(r)/dr = -\rho^2(r)g(r)/K_S(r) \tag{4}$$

where $K_S(r) = \rho(\partial P/\partial\rho)_S$ is the isentropic bulk modulus and G is the gravitational constant. We write K_S in terms of the isothermal bulk modulus K_T as,

$$K_S(r) = K_T(r)[1 + \alpha(r)\gamma(r)T(r)] \tag{5}$$

where α is thermal expansivity, γ is the Gruneisen parameter, and T temperature. The equation of state (EOS) we use to relate K_T to ρ is the third order Vinet EOS (Oganov,

2007; Vinet et al., 1989),

$$K_T = K_0 x^{-2/3}[1 + (1 + \theta x^{1/3})(1 - x^{1/3})]\exp[\theta(1 - x^{1/3})] \quad (6)$$

where the zero subscript refers to the zero pressure value of a quantity, $x(r) = \rho(r)/\rho_0$, and $\theta = 3/2(K_0' - 1)$, where K_0' is the zero pressure derivative of K_T. The adiabatic temperature gradient,

$$dT_{ad}(r)/dr = -\rho(r)g(r)\gamma(r)T(r)/K_S(r) \quad (7)$$

describes the increase in temperature with depth in a well-mixed layer. The depth-dependence of the remaining thermodynamic parameters γ and α are parameterized by

$$\gamma(r) = \gamma_0(x(r))^{-\gamma_1} \quad , \quad \alpha(r) = \alpha_0(x(r))^{-3} \quad (8)$$

where γ_0, γ_1, and α_0 are constant within each compositional layer (Table 1). The variation of α with density in (8) is similar to that of Chopelas and Boehler (1992) derived from experiments at high pressure and temperature.

We impose surface conditions on each model of $P_0 = 1$ atm, $\rho_0 = 3226$ kg m^{-3}, and $T_0 = 300$ K. Conditions at the center ($r = 0$) of each model require that the mass and gravity go to zero and the other variables (e.g. ρ and T) remain smooth and finite. The internal structure equations (1)-(8) are integrated from the surface inwards and the surface radius R is modified until the conditions are satisfied at the center, with a typical error in R that corresponds to about one part in 10^4.

2.1 Layers

We include up to 5 layers in the model: a peridotite upper mantle, a perovskite mid-mantle, a post-perovskite lower mantle, and a solid or liquid metallic core. Our models do not include a spinel structure as in the transition zone of the Earth's mantle, because this

layer is less than 300 km thick. There are 4 possible transitions or discontinuities: peridotite to perovskite, perovskite to post-perovskite in the mantle, a core-mantle boundary (CMB) where the material changes from silicates to iron, and an iron solidus boundary denoted the inner core boundary (ICB). The pressure at which the olivine transitions to perovskite (in the spinel structure) is a function of temperature described by (Ito and Takahashi, 1989)

$$P(T) = P_{pd0} - \gamma_{pd} T \tag{9}$$

where the reference pressure is $P_{pd0} = 28.3$ GPa and the Clapeyron slope is $\gamma_{pd} = 2.8$ MPa K^{-1}. The pressure at which perovskite transforms to the higher density post-perovskite phase is described by

$$P(T) = P_{ppv0} + \gamma_{ppv}(T - T_{ppv0}) \tag{10}$$

where the reference pressure and temperature are $P_{ppv0} = 124$ GPa and $T_{ppv0} = 2500$ K, and the Clapeyron slope is $\gamma_{ppv} = 8$ MPa K^{-1} (Hernlund and Labrosse, 2007).

The core-mantle boundary r_{cmb} is defined as the radius at which the mass above r_{cmb} is equal to the prescribed mantle mass $M_m = M(1 - \mathrm{CMF})$, where M is the total planet mass and we assume a core-mass fraction (CMF) of either 0.32 (Earth-like) or 0.65 (Mercury-like). The iron core can be completely molten, completely solid, or partially molten with a liquid or solid shell depending on where the core temperature profile intersects the iron solidus. We define the iron solidus by Lindemann's Law (Poirier, 1991)

$$T_{melt} = T_{Fe0} exp[2\gamma_0(1 - 1/x) + 2/3 \ln(1/x)] \tag{11}$$

where $T_{Fe0} = 1811$ K is the zero pressure melting temperature of iron (Weast, 2009) and $\gamma\rho \approx \gamma_0\rho_0$. Depending on the relative slopes of the core geotherm and the iron melting curve, the core may have a liquid shell with a solid inner-core as in the Earth, or vice versa, or the core may be entirely liquid or solid.

2.2 Material properties

With 4 possible discontinuities there are 5 distinct layers. The thermodynamic properties of the candidate materials, which can be discontinuous across boundaries, are uncertain despite the significant constraints provided by high pressure experiments. As a consequence of these large uncertainties, seismically consistent Earth structure models have been constructed over a range of parameter values. We use a set of zero pressure constants, shown in Table 1, that produce an Earth model internal structure as close as possible to the preliminary Earth reference model (PREM) by Dziewonski and Anderson (1981) and the geotherm constructed by Stacey (1992). More recent estimates of the core melting curve by Alfe et al. (2003) suggest that temperatures may be ~ 600 K hotter than the ICB temperature of 5000 K estimated by Stacey (1992).

The thermal conductivity in the mantle is assumed to vary with pressure as (Van den Berg et al., 2002),

$$k = k_0(1 + PK_0'/K_0) \tag{12}$$

where $k_0 = 3.3$ $\mathrm{WK^{-1}m^{-1}}$, which closely approximates the model of Hofmeister (1999). The adiabatic heat flow out of the core depends on the thermal conductivity of iron and thermal gradient at the top of the core. For the core thermal conductivity we use the Wiedemann-Franz Law $k = \sigma LT$ where $\sigma = 3 \times 10^5$ $\mathrm{Sm^{-1}}$ is the assumed electrical conductivity of the outer core, $L = 2.5 \times 10^{-8}$ $\mathrm{WS^{-1}K^{-2}}$ is the Lorentz Number (Poirier, 1991; Stacey and Loper, 2007), and T is the absolute temperature.

3 Thermal model

Previous super-Earth internal structure models have imposed simplified thermal profiles that assume temperature jumps in the thermal boundary layers based on those found in the Earth (e.g. Valencia et al., 2006; Sotin et al., 2007), or alternatively have ignored any non-

adiabatic thermal contribution since it has a minor influence on the planetary radius and density (e.g. Seager et al., 2007). In this section we describe a whole planet thermal model that can both reproduce the geotherm of the Earth for a 1 M_E model, referred to here as simply the Earth model, and also produce optimal thermal profiles for a range of masses and CMFs that maximize the core heat flow.

Our fundamental assumption is that the mantle and core are in thermal equilibrium, so that the heat flux through the surface equals the sum of the heat flux from the core plus the internal heat loss from the mantle. For the optimal dynamo models considered here, secular cooling and radioactive heating are set to zero so there are no internal heat sources. Thermal equilibrium also requires that the temperature profile be smooth and continuous. In this scenario, convection in the mantle determines the steady-state heat flux both at the surface of the planet and at the CMB.

To investigate the most energetically favorable, or optimal thermal structure, we assume that both the mantle and core are convecting vigorously, such that within each convective region away from boundary layers the material is well-mixed and the temperature gradient is adiabatic. The temperature jumps at each boundary layer are determined by assuming optimal sub-solidus mantle convection where the temperature profile in the thermal boundary layers is just beneath the mantle solidus. If the average geotherm at a given depth were to exceed the mantle solidus then substantial melting would occur, creating a convective instability, then the excess heat would be advected away in a short time and the boundary layer would return quickly to a dynamically stable, slightly sub-solidus temperature. Although this argument requires that the average geotherm be sub-solidus, it does not rule out localized regions of melting, as occur in the Earth.

3.1 Optimal state

For convenience we separate the full temperature profile $T(r)$ into a super-adiabatic (convective) component T_{conv} and adiabatic correction T_{ad} so that $T(r) = T_{conv}(r)+T_{ad}(r)$. In thermal boundary layers, conduction is the dominant contribution to the heat transfer so we use the error function solutions to the heat equation to describe the convective temperature profiles in the upper and lower mantle,

$$T_1(r) = T_0 + \Delta T_1 \mathrm{erf}\left(\frac{R-r}{\delta_1}\right), \text{ for } R \geq r \geq r_{mid} \tag{13}$$

$$T_2(r) = T_{mid} + \Delta T_2 \mathrm{erfc}\left(\frac{r-r_{cmb}}{\delta_2}\right), \text{ for } r_{mid} \geq r \geq r_{cmb} \tag{14}$$

where the subscripts 1 and 2 refer to the upper and lower mantle thermal boundary layers, respectively, r_{mid} is the mid-mantle radius, $\Delta T_1 = (T_{mid} - T_0)$ and $\Delta T_2 = (T'_{cmb} - T_{mid})$ are the boundary layer temperature jumps, and δ is the thermal boundary layer thickness. The temperature at the mid-mantle is T_{mid} and at the CMB is $T'_{cmb} = T_{cmb} - T_{ad,cmb}$, where $T_{ad,mid}$ is the adiabatic temperature contribution at the mid-mantle, so that T_{mid} and T'_{cmb} have the adiabat removed. The convective temperature profile is then given by $T_{conv}(r) = T_1(r)+T_2(r)$, so that $T_{conv} = T_1 = T_2$ at r_{mid}. To specify the mantle geotherm we solve for the unknown variables T'_{cmb}, T_{mid}, δ_1, and δ_2 in (13,14) subject to three dynamical constraints: (i) The local Rayleigh number is critical for convection in the upper mantle thermal boundary layer; (ii) The geotherm in the upper and lower mantle thermal boundary layers are at the local melting temperature; (iii) The core and mantle are in thermal equilibrium so that the total surface heat flow is the sum of the internal heat produced in the mantle plus the heat leaving the core. We refer to models that meet these three dynamical constraints as in the *optimal state for thermal convection in the core*. The method used to solve for the remaining unknowns by applying these constraints to the thermal boundary layers in (13,14) is described below.

3.2 Mantle solidus

To specify the melting temperature throughout the mantle as a function of pressure we use the mantle solidus for the two major mantle constituents in this model: peridotite and perovskite. We use a dry peridotite melting curve derived from a compilation of piston cylinder and multianvil experiments (Hirschmann, 2000) of the form

$$T_{melt} = T_{pd0} + 90P \ , \ \text{for } P < 16 \text{ GPa} \tag{15}$$

where P is in GPa, T is in K, and $T_{pd0} = 1373$ K. We construct a melting curve for perovskite in lower mantle (Zerr et al., 1998; Oganov, 2007) of the form

$$T_{melt} = T_{pv0} + 400(P-5)^{1/2} \ , \ \text{for } P > 16 \text{ GPa} \tag{16}$$

where P is in GPa and $T_{pv0} = 1500$ K. The two equations are constructed to give the same melting temperature at 16 GPa.

3.3 Mantle temperatures

In our optimal models the CMB temperature is set to the mantle melting temperature $T_{cmb} = T_{melt}(P_{cmb})$. Our Earth model uses the presently preferred value of $T_{cmb} = 4000$ K. An otherwise similar model that allows the lower most mantle to be at the perovskite melting temperature of $T_{cmb} \approx 6000$ K is referred to as the optimal Earth-mass model. This model may be representative of the early Earth when T_{cmb} was just below the silicate solidus, following magma ocean solidification (Schubert et al., 1979). (See §7 for a discussion of application to the ancient terrestrial planets.)

The assumption that the lower mantle is made up of only perovskite, with no (Fe,Mg)O, has implications for the melting temperature at the CMB. High pressure experiments and theoretical ab initio calculations of the melting properties of MgO at CMB pressures indicates

melting begins around 5500 K, and is substantially less than the solidus of perovskite at these pressures (Boehler, 2007). However, if (Fe,Mg)O and perovskite are mixed near the eutectic composition at the CMB then melting may occur at even lower temperatures of $\sim$ 4300 K (Holland and Ahrens, 1997). Recently it has been proposed that a thin (Fe,Mg)O melt layer at the base of the mantle may be negatively buoyant compared to the surrounding solid lower mantle and therefore dynamically stable (Mosenfelder et al., 2007). Modifying the solidus curve of the lower mantle in (16) will not change the optimal core heat flow Q_c calculated below because Q_c is related to the upper mantle boundary layer heat flow, which is determined by the better constrained upper mantle peridotite solidus in (15).

The mid-mantle temperature defined in (13,14) is fundamentally limited by the shape of the error function describing the thermal boundary layers and the mantle solidus. If mantle temperatures were to greatly exceed the melting curve then either large scale melting would occur and the excess heat would be rapidly convected away, or the core would be superheated. Although neither case is thermodynamically stable, the rate at which the mantle and core would reach an equilibrium state is dependent on the heat transfer at the CMB and the efficiency of mantle convection, and some disequilibrium could persist over geological time scales.

We define the depth at which the upper mantle temperature profile T_1 touches the silicate melting curve T_{melt} as z_{melt}. In general, this depth could be a fraction of the thermal boundary layer thickness so that $z_{melt} = \xi\delta_1$, where ξ is between 0 and 1. A small ξ implies that melting occurs close to the surface, which will produce a larger melt region. For simplicity we choose $\xi = 1$ so that $z_{melt} = \delta_1$, which produces a thin layer of melt just below z_{melt} due to the shape of the error function (see Figure 1). To solve for z_{melt} we equate $T_1(z_{melt})$ and $T_{melt}(z_{melt})$ giving,

$$T_{mid}(z_{melt}) = T_0 + \frac{1}{\mathrm{erf}\xi}[T_{melt}(z_{melt}) - T_{ad}(z_{melt}) - T_0] \tag{17}$$

where we have used (13,14) and $\Delta T_1 = T_{mid} - T_0$. To determine z_{melt} we invoke dynamical constraint (i) requiring that $Ra(\delta_1) = Ra_{crit}$. The Rayleigh number is defined as

$$Ra = \frac{\alpha g \Delta T \delta^3}{\kappa \nu} \tag{18}$$

where ΔT is the temperature jump across the depth interval δ. We use $\kappa = 10^{-6}$ m^2 s^{-1} for thermal diffusivity and a characteristic dynamic viscosity of the upper mantle that is consistent with thermal history models to be around $\eta = 2\times10^{20}$ Pa s (Labrosse and Jaupart, 2007; Davies, 2007), giving a kinematic viscosity of $\nu = \eta/\rho_0 = 6.2 \times 10^{16}$ m^2 s^{-1}. This upper mantle viscosity is assumed to be constant in all models, whereas a more realistic viscosity should be temperature dependent, possibly following an Arrhenius law type of temperature dependence (e.g. Kohlstedt, 2007; Davies, 2007).

Equations (17) and (18) each give a relation for ΔT_1 as a function of δ_1, and the intersection of these relations provides a unique solution for both parameters. The convective temperature jump in the lower mantle thermal boundary layer is then given by $\Delta T_2 = T'_{cmb} - T_{mid}$, the temperature jump required to go from the mid-mantle to CMB temperature.

3.4 Heat flow

The heat flow through the upper and lower mantle thermal boundary layers are, respectively,

$$Q_1 = \frac{2}{\sqrt{\pi}} A_1 k_1 \frac{\Delta T_1}{\delta_1} \ , \ Q_c = \frac{2}{\sqrt{\pi}} A_2 k_2 \frac{\Delta T_2}{\delta_2} \tag{19}$$

where A_1 and A_2 are the areas of the planet surface and CMB, respectively, k_1 and k_2 are the thermal conductivities in the mantle at these boundaries, and the numerical factor $2/\sqrt{\pi}$ comes from the derivative of the error function. We separate the total surface heat flow into two sources:

$$Q_1 = Q_R + Q_c \tag{20}$$

where Q_R is the radioactive heat production in the mantle and Q_c is the core heat flow defined in (19). We note that secular cooling may be included into Q_R because both radioactivity and secular cooling can be written as volumetric source terms in the mantle energy balance (Nimmo, 2007). We specify the radioactive heat flow by choosing a homogeneous heat production rate H in units of [W kg^{-1}], so $Q_R = HM_m$, where M_m is the mass of the mantle. For a given heat production rate and surface heat flow, the core heat flow Q_c is determined by (20).

Given Q_c and ΔT_2 we solve for the lower mantle boundary layer thickness from (19),

$$\delta_2 = \frac{2}{\sqrt{\pi}} A_2 k_2 \frac{\Delta T_2}{Q_c} \tag{21}$$

We now have all the mantle properties needed to construct the convective temperature profiles defined in (13,14).

3.5 Earth model

To construct a convective mantle profile for the present-day Earth, the steps just described are slightly modified as follows. For the present-day Earth we subtract from the total surface heat flow the radioactivity of the continental crust, which does not enter into the mantle dynamics. This gives $Q_1 = 40$ TW for the surface mantle heat flow. We assume the CMB temperature $T_{cmb} = 4000$ K and a radioactive heat production density in the mantle of $H = 7.5 \times 10^{-12}$ W kg^{-1}. Given the mass of the Earth's mantle, this implies a total internal heat generation of $Q_R \approx 30$ TW, so that $Q_c \approx 10$ TW from (20). We note that a recent estimate by Jaupart et al. (2007) actually partitions the mantle heat loss of 30 TW into a radioactive heat generation of 20 TW and secular cooling of 10 TW. We do not need to invoke the critical Rayleigh number condition in order to solve this system, although the Rayleigh number it produces is in fact close to the critical value. The remaining unknowns are then found the same way as the optimal model described above.

Figure 1 shows the temperature profile of the Earth model in solid black, the mantle and core melting curves defined in (15), (16), and (11) in grey, the convective profile T_{conv} defined by (13,14) as a dashed line, and the adiabatic correction defined in (7) as a dotted line. The adiabatic temperature correction shown in Figure 1 is equal to the difference between T and T_{conv}. Note that T_{conv} is defined so that it is isothermal in the convective regions of the mantle and core and increases only in the upper and lower mantle thermal boundary layers. We define the adiabatic heat flow from the core as Q_{ad} and the super-adiabatic heat flow available to drive convection there as $Q_{conv} = Q_c - Q_{ad}$. For the Earth model with $\xi = 1$ we find $z_{melt} = \delta_1 = 71.2$ km, $\Delta T_1 = 1498$ K, $Q_1 = 39.9$ TW, $Q_R = 30.2$ TW, $\delta_2 = 286$ km, $\Delta T_2 = 1564$ K, $Q_c = 9.7$ TW, $Q_{ad} = 2.4$ TW, and $Q_{conv} = 7.2$ TW. Since we specify Q_1, Q_R, and T_{cmb} in this model we calculate the Rayleigh number in the upper thermal boundary layer, instead of setting it to Ra_{crit}, and find $Ra_1 = 1342$, which is super-critical for convection in the mantle.

Including mantle heat production due to radioactivity in the Earth model requires that more heat flow through the upper mantle boundary layer than the lower boundary layer, in this case by about a factor of 4. Physically this condition requires that the upper boundary layer thickness δ_1 be smaller than δ_2, although it can also be satisfied by changing the ratio of ΔT_1 to ΔT_2 because there is a trade-off between ΔT and δ in the heat flow (19).

4 Magnetic field scaling law

The onset of dynamo action by convective flow in an electrically conductive fluid is an instability analogous to the onset of convection that occurs as the Rayleigh number, or convective forcing, is increased beyond a critical value that depends on other fluid parameters such as the rotation rate and the magnetic diffusivity. Specifically the onset of self-sustained magnetic field generation occurs in rapidly rotating convection when the magnetic Reynolds number of the flow $Rm = vD/\eta_m$ exceeds a critical value of $Rm_{crit} \simeq 40$, where D is

shell thickness and η_m is the magnetic diffusivity (Roberts, 2007). Later we show that, for reasonable rotation rates, most models with a partially liquid core and a positive superadiabatic core heat flow are supercritical for both convection and dynamo action.

Relating the magnetic field intensity of the dynamo to physical properties of the convecting fluid has been a challenge for several decades and a number of scaling laws have been proposed (e.g. Olson et al., 2009; Griessmeier et al., 2004). An early proposal by Elsasser (1946) was that the dynamo-generated magnetic field saturates at an intensity that is determined by an equilibration between the Coriolis and Lorentz forces, known as a magnetostrophic balance. This balance holds when the Elsasser number $\Lambda = \sigma B^2/\rho\Omega$ is of order one, where σ is electrical conductivity and Ω is planetary rotation rate. Sanchez-Lavega (2004) used the Elsasser number to predict the magnetic field intensity of giant extrasolar planets, and Griessmeier et al. (2004) used this and other scaling laws to estimate the extent to which the magnetic field of a hot jupiter might influence atmospheric loss rates. Despite the importance of the magnetostrophic balance in dynamos, it is known that Λ varies by over an order of magnitude for the magnetic planets in the Solar System (Olson and Christensen, 2006), with dipole based values of $\Lambda \sim 5 \times 10^{-2}$ for the Earth and Jupiter and $\Lambda \sim 10^{-3} - 10^{-5}$ for the other magnetic planets. In addition, the Elsasser number criteria is at variance with numerical dynamo results, which show that the intensity of a convectively generated magnetic field becomes independent of the rotation rate in the limit of fast rotation.

Recently it has been proposed that a single scaling law that is proportional to the energy flow through the dynamo region of the form $B \propto (DF)^{1/3}$, where D is dynamo region shell thickness and F is buoyancy flux, can be used to estimate the dipolar dominant magnetic field intensities of the planets in the Solar System, fast rotating M stars, and numerical dynamo models over a huge range of parameter space (Christensen and Aubert, 2006; Christensen et al., 2008, 2009). The exponential dependence of 1/3 can be determined from a simple dimensional analysis, assuming independence of the diffusivities and rotation rate assuming

it is sufficiently fast. First rewrite B by balancing the advection and Lorentz force terms in the conservation of momentum which gives an expression for the Alfven velocity $v_A \sim B/\sqrt{\rho\mu_0}$. The unique relationship between v_A in units of [m s^{-1}], F in units of [m^2 s^{-3}], and D in units of [m], is $v_A \sim (DF)^{1/3}$. The success of this scaling law in predicting magnetic field strengths over many orders of magnitude demonstrates that magnetic field intensity is determined by the energy flux through the dynamo region and that it cannot grow indefinitely with rotation rate. In addition, the rotation rates of the dipolar-dominant magnetic planets in the Solar System, specifically Earth, Jupiter, and to a lesser extent Saturn, are sufficient for this law to apply.

We adopt a form of this scaling law from Olson and Christensen (2006) for the rms dipole field intensity at the CMB,

$$B_c = \gamma_d(\rho\mu_0)^{1/2}\left(r_{cmb}F\right)^{1/3} \tag{22}$$

where $\gamma_d = 0.2$ is the saturation constant for fast rotating dipolar dynamos, $\mu_0 = 4\pi \times 10^{-7}$H m^{-1} is magnetic permeability, $F = \alpha g q_{conv}/\rho c_p$ is the buoyancy flux, q_{conv} is the convective heat flux, and we have modified the law to include entirely liquid cores. Substituting for F gives,

$$B_c = \gamma_d(\rho\mu_0)^{1/2}\left(\frac{\alpha g}{\rho c_p} r_{cmb} q_{conv}\right)^{1/3} \tag{23}$$

The rms dipole field intensity at the core surface is projected to the planet surface by,

$$B_s = B_c(r_{cmb}/R)^3 \tag{24}$$

and related to the magnetic moment by,

$$\mu = 4\pi r_{cmb}^3 B_c/\sqrt{2}\mu_0 \tag{25}$$

which is an intrinsic and directly measurable property of a planetary dynamo. For the Earth model described in §3.5, using $\gamma_d = 0.17$, we find $\mu = 83$ ZAm^2, $B_c = 0.27$ mT, and $B_s = 0.032$ mT. These values agree well with present-day measurements of the geomagnetic dipole field.

5 Results

For each combination of planet mass and core mass fraction (CMF) considered we create a self-consistent whole planet model by iterating between the internal structure model with a fixed temperature profile and the optimal thermal model with a fixed internal structure until additional iterations produce negligible changes in both. The last step is to apply the magnetic field scaling law.

5.1 Internal structure

Figure 2 shows the density (2a,b) and pressure (2c,d) profiles for 32% and 65% CMF and $1 - 10$ M_E optimal models, along with the present-day Earth model (labeled E) for comparison. The density jump in the Earth model associated with the ICB is the only visible departure from the optimal 1 M_E model, the later being too hot to freeze out a solid inner core. In fact, for all optimal models the core is hot and entirely liquid. Ongoing solidification of the Earth's inner core provides a release of light elements at the ICB that is a source of gravitational energy available to drive core convection. Light element buoyancy production at the ICB is estimated to provide at least one half of the entropy available to drive the geodynamo (Gubbins et al., 2004) and is about five times more thermodynamically efficient than thermal buoyancy (Roberts et al., 2003). The absence of inner core solidification in the optimal models requires that core convection and dynamo action be maintained by thermal convection alone.

As expected in the 65% CMF models, the cores are larger while the surface radii are

smaller because the iron core is much more dense than the silicate mantle. The density jumps in the optimal models in Figure 2 are associated with the pressure induced silicate phase transitions in the mantle and the silicate-iron interface at the CMB.

5.2 Thermal structure

Optimal whole planet temperature profiles are shown in Figure 3. In general, the CMB temperature is hotter in the 32% CMF models than those with larger cores because the melting law in (16) is proportional to P_{cmb}, which is larger for 32% CMF models because the CMB is deeper. The optimal Earth-mass model is hotter than the Earth model (bottom curve in Figure 3a) because in the Earth model the CMB temperature is set to the seismically inferred value of 4000 K, which is considerably lower than the CMB melting temperature for perovskite of $T_{cmb} \approx 6000$ K. The mid-mantle temperature in the Earth model is nearly as hot as in the optimal model due to internal heat production.

Thermal properties for the upper mantle and lower mantle boundary layers are shown in Figures 4 and 5, respectively. The optimal surface heat flow is strongly constrained by the upper mantle melting curve and the critical local Rayleigh number assumption. These constraints limit ΔT_1 to about $1100 - 1300$ K and δ_1 to about $60 - 40$ km even though T_{cmb} increases with planet mass. One effect of these constraints is that most of the convective temperature increase needed to reach T_{cmb} must occur in the lower mantle thermal boundary layer. The surface heat flow Q_1, shown in Figure 4c, for the Earth-mass optimal model is similar to the Earth model because the Earth model is close to the optimal state as defined here. Also, Q_1 is slightly larger for the 32% CMF models because the surface area is larger, despite the fact that the average surface heat flux $q_1 \sim k_1 \Delta T_1 / \delta_1$ is larger for 65% CMF. Figure 4d confirms that the Rayleigh number in the upper mantle Ra_1 is set to Ra_{crit} in the optimal models.

Figure 5 shows the thermal properties in the lower mantle boundary layer. As expected,

the temperature jump there ΔT_2 is larger and varies more with mass than ΔT_1 because of its dependence on T_{cmb}. The CMB heat flow is equal to the surface heat flow in the optimal models because there is no internal heat source in the mantle. This is an extreme limit, as some amount of radioactivity and secular cooling is likely, which would tend to decrease Q_c. In the optimal models the lower boundary layer thickness is a free parameter that is constrained by the CMB heat flow according to (21), and varies in proportion to ΔT_2. The Rayleigh number in the lower boundary layer Ra_2 is larger than Ra_1 because it increases as $\sim \Delta T_2 \delta_2^3$. We note that in the calculation of Ra_2 we have assumed that $\alpha g/\nu\kappa$ is equal in the two boundary layers, but a systematic increase in ν in the lower mantle of order $\sim 10^3$ (as is thought to occur in the Earth) would bring the value of Ra_2 down closer to Ra_{crit}.

5.3 Surface age

A compelling feature of optimal mantle convection, or any mobile lid convection, is the influence the upper thermal boundary layer may have on the recycling rate of surface materials. In the mobile-lid regime surface tectonics are driven by the large scale convective motions of the upper mantle, but the connection between surface motions and mantle flow is a complex function of composition and rheology, and is not fully understood even in the case of the Earth (Schubert et al., 2001; Bercovici, 2003). If the optimal models described here produce surface tectonics similar to that on the Earth then we can say something about the typical time and length scales of surface processes.

In situ measurements of the Earth's oceanic crust show that for seafloor younger than 80 Myr the decrease in heat flux with mean crustal age τ is consistent with a simple half-space cooling model of the form $q \propto \tau^{-1/2}$ (Jaupart et al., 2007). Physically this says that where the upper mantle thermal boundary layer is thicker the oceanic crust is older and colder.

In the half-space cooling model, mean crustal age is equated with the thermal diffusion time through the conductive thermal boundary layer with thickness δ_T, which is the depth

at which partial melting occurs. For this calculation we assume this occurs 40% deeper than the depth predicted by our dry peridotite solidus in (15) due to the presence of water, which tends to depress the melting curve (Hirth and Kohlstedt, 1996; Karato and Jung, 1998). With $\delta_T = 1.4\delta_1$ we solve for the mean crustal age as a function of the upper mantle boundary layer thickness as (Turcotte and Schubert, 2002),

$$\tau = \frac{(\delta_T/2)^2}{\kappa} \tag{26}$$

where $\kappa = 10^{-6}$ m^{2}s^{-1} is thermal diffusivity. If we further assume, for example, a convective planform with an average wavelength of $\lambda = 2\pi R/m$, where $m = 5$ is the dominant mode of the planform, then we may estimate the mean surface velocity

$$u = \frac{\lambda/2}{\tau} \tag{27}$$

corresponding to the length of a cell equal to $\lambda/2$.

For the Earth model with (26) and (27) we find $\delta_T = 100$ km, $\tau = 78$ Myr, $\lambda = 8000$ km, and $u = 50$ mm yr^{-1}, similar to average present-day oceanic crust values. Figure 6 shows that our optimal model predicts younger and faster plates on average compared to the Earth. We emphasize that this calculation is merely illustrative, and we are not relying on the assumption that some form of Earth-like plate tectonics is active at the surface, nor are we arguing that this should be the case, which is a topic of recent controversy (Valencia et al., 2007; O'Neill et al., 2007).

5.4 Core convection

To maintain convective dynamo action in the core of a planet without a solidifying inner core, the average CMB heat flow must exceed the adiabatic heat flux. The rate at which heat is extracted from the core is limited by the lowermost mantle boundary layer, the D"

layer in the Earth, in at least two ways: (1) the thermal conductivity is probably much lower than that of the iron rich core, and (2) the temperature gradient is controlled by the slow convective processes in the mantle. Current seismically inferred estimates of the CMB heat flow $\sim 10 \pm 4$ TW (Lay et al., 2006; Van der Hilst et al., 2007) are larger than estimates of the core adiabatic heat flow $\sim 3 - 4$ TW, implying that convection in the Earth's outer core is driven at least in part by thermal gradients.

The convective (or super-adiabatic) heat flow Q_{conv}, shown in Figure 7, is positive for all optimal models, consistent with thermal convection in each case. Q_{conv} is larger in the 32% CMF models because they maintain a larger total heat flow at the core surface and require about half the adiabatic core heat flow of the 65% CMF models. The ratio Q_{conv}/Q_{ad} varies from $1 - 5$ in the 32% CMF models, and from $0.3 - 2$ in the 65% CMF models. Therefore, thermal convection is expected to be more rigorous in the 32% CMF models, although as we will see below the magnetic field strength is both a function of heat flux and size of the dynamo region, which is larger in the 65% CMF models.

Due to the fact that the optimal models are too hot to freeze a solid inner core, there is no gravitational energy source available to assist core convection. In the early Earth, before the nucleation onset of the inner core, thermal convection may have powered the dynamo alone. Roberts et al. (2003) estimated that a superheated core could cool to an adiabatic state in ~ 0.5 Gyr. This time scale will likely increase with mean core temperature, and therefore with mass in the optimal models, but in any case it ultimately leads to inner core freezing even for an initially hot core. To estimate the typical core secular cooling times we use

$$-\frac{dT_c}{dt} = \frac{Q_c}{M_c c_p} \tag{28}$$

where T_c is the mean core temperature, M_c is core mass, and core heat capacity is $c_p = 1000$ J kg^{-1}K^{-1}. For $1-10$ M_E models with 32% CMF we find $-dT_c/dt = 500-300$ K Gyr^{-1}, which corresponds to a fractional a decrease of 35-10% in the core temperature over 4.5 Gyr.

For models with larger 65% CMF, the secular cooling rate and fractional decrease in core temperature over 4.5 Gyr is about half that of the 32% CMF models. Planets with smaller cores tend to evolve faster, whereas larger cores generally cool more slowly because they can retain more primordial heat. This is an upper estimate of the core secular cooling rate because radioactive heating in the mantle and sub-optimal mantle convection would lead to a decrease in the CMB heat flow.

5.5 Magnetic field

As demonstrated in Figure 7a the heat flux at the top of the core is super-adiabatic in all models and, assuming a fast planetary rotation rate (similar to the Earth's), we expect a convecting iron core to maintain dynamo action and a large-scale dipolar magnetic field. As a check, we calculate the magnetic Reynolds number for each model using $Rm = u_c r_{cmb}/\eta_m$, where u_c is the convective velocity in the core and the magnetic diffusivity is $\eta_m = 2$ m^{2}s^{-1} (Jones, 2007). We use the scaling relation derived by Olson and Christensen (2006) to relate the convective velocity to the buoyancy flux

$$u_c \simeq 1.3(r_{cmb}/\Omega)^{1/5} F^{2/5} \tag{29}$$

which gives strongly supercritical magnetic Reynolds numbers of $Rm \sim 10^4$ for the optimal models. The same relation gives $Rm \sim 2500$ for the geodynamo, which is about twice the typical estimates (Christensen and Tilgner, 2004) because the numerical coefficient in (29) is about twice as large for base-heated dynamos compared to internally heated dynamos.

To calculate the magnetic field intensity we use the scaling laws in (23), (24), and (25), with $\gamma_d = 0.2$. Figure 7 shows (b) the magnetic moment μ, and the magnetic field at (c) the top of the core B_c and (d) the planet surface B_s, in geomagnetic units. A scaling law is

plotted (grey) for the magnetic moment as a function of mass and CMF of the form,

$$\mu = \mu_1(\mathrm{CMF}/0.32)^{c_1}(M/M_E)^{c_2} \tag{30}$$

where μ_1 is the magnetic moment of the optimal 1 M_E, 32% CMF model, and the exponents are $c_1 = 1.3$, and $c_2 = 0.85$ or 0.65 for the 32% or 65% CMF models, respectively. A similar scaling law for the planet radius is constructed with exponents $c_1 = -0.12$ and $c_2 = 0.27$.

The magnetic field intensity at the CMB is slightly stronger for the 32% core dynamos because of a higher convective heat flow, but B_c is confined to a modest $2 - 2.5$ times the geomagnetic field strength for all cases. For larger cores the dynamo region is closer to the planetary surface so B_s exceeds the 32% CMF surface fields by about a factor of 2.5. The magnetic moment is a strong function of core size, which increases with mass and CMF, thus producing a magnetic moment up to 23 times the geomagnetic dipole moment for a 10 M_E planet with a large core. For even larger planet masses and cores than those considered here we expect little change in the magnetic field intensity at the CMB and only modest increases in μ according to the trends in Figure 7. Important material properties, such as thermal conductivity, at ultra high pressures and temperatures are so uncertain that extrapolation to even larger planets becomes questionable.

6 Detectability

A promising way to gain new insights into the interior of terrestrial exoplanets is by observation of their magnetic fields. The magnetic fields of the giant planets in the Solar System were first remotely detected by their electron cyclotron emission at radio frequencies. In fact, the oscillation of such emissions caused by non-axisymmetric field components is commonly used to define the rotation periods of the gas planets, whose surfaces rotate differentially (Guillot, 2005; Gurnett et al., 2007). Predictions of radio emission from extra-

solar magnetic fields (Yantis et al., 1977; Lecacheux, 1991) predate the detection of the first exoplanet in 1995.

Electron cyclotron emission is caused by energetic solar wind particles interacting with planetary magnetic field lines, generating radiation at the electron cyclotron frequency

$$f_c = eB_s/2\pi m_e \tag{31}$$

where e and m_e are electron charge and mass. The emission power depends on the solar wind density, planetary magnetic field strength, and semi-major axis. In application to the magnetic planets in the Solar System, Desch and Kaiser (1984) developed a "radiometric Bodes law" for emission power as a function of magnetic moment and distance. We use a version of this law of the form (Farrell et al., 1999)

$$P_{rad} = \left(\frac{\mu}{\mu_J}\right)^{0.58} \left(\frac{a_J}{a}\right)^{1.17} \times 4 \times 10^9 \text{ W} \tag{32}$$

where a is semi-major axis, subscript J refers to Jupiter, and the constant coefficient on the right is proportional to the intensity of the solar wind. The radio flux observed at the Earth is the emission power divided by the spherical area of projection,

$$\Phi = P_{rad}/4\pi s^2 \Delta f \tag{33}$$

where s is the distance to the planet from Earth and Δf is the observational bandwidth, assumed here to be $f_c/2$.

Figure 8 shows the cyclotron emission power versus frequency for a number of terrestrial exoplanets assuming they are in an optimal state and have a large 65% core mass fraction. The exoplanets shown, GJ674b (11.7 M_E), GJ581b (15.6 M_E), GJ581e (1.94 M_E), 55Cnc e (7.63 M_E), and HD7924b (9.22 M_E), all orbit within $a = 0.1$ AU and are less than $s = 17$ pc away (see Schneider, 2010). Figure 8 also shows the potential emission from exoplanets

with $1 - 10\ M_E$ and 32% or 65% CMF orbiting at $a = 0.02$ AU around the stars GJ876 ($s = 4.72$ pc) and α Centauri ($s = 1.33$ pc), and the emission from Earth, Jupiter, and Saturn if they orbited α Centauri. The detection threshold expected for the Low Frequency Array (LOFAR), the most sensitive ground-based radio telescope (Kassim et al., 2004), for an 8 hour observing time is far from the ability to detect even the most favorable targets. Futhermore, due to the fact that the Earth's ionosphere blocks emissions with frequencies less than ~ 10 MHz (~ 3 MHz in polar regions), detection of magnetic fields in terrestrial exoplanets is unlikely with ground-based radio telescopes.

More promising mechanisms that would boost the amplitude of the cyclotron emission include more intense solar wind or solar flares, which provide a temporary burst of solar wind intensity. The closest stars are generally chromospherically quiet like our Sun, so that periodically flaring or younger more active stars may be better targets. Alternative boosts and modulations to the emission amplitude may be generated by a highly eccentric orbit, where solar wind intensity would be a maximum at periastron, or by interaction with another nearby magnetic planet. For example, there is a periodic modulation of Jupiter's decametric emission at the orbital period of Io due to a uni-polar magnetic interaction between the Jovian field and the moon (Zarka, 2007). In dynamically crowded planetary systems like GJ876 interaction between multiple planetary magnetic fields may also modulate the emission at regular, resonant intervals.

Several groups are currently searching for magnetospheric emissions from hot-Jupiter exoplanets, which are expected to have stronger magnetic fields and emit at higher frequencies (e.g. Farrell et al., 2004; Lazio et al., 2010). Although no emission from an exoplanet magnetic field has yet been found, the lower limits on the observable emission intensity are approaching the range of intensities predicted by dynamo theory for such planets.

7 Ancient terrestrial planets

Of the four terrestrial planets in the Solar System only Earth and Mercury presently maintain core dynamos, although Mercury's magnetic field is anomalously weak and may be fundamentally different than the geodynamo (Anderson et al., 2008; Christensen, 2006). On Mars there is evidence for ancient remnant magnetization of surface rocks indicating that it likely maintained a core dynamo in its past (Acuna et al., 1998). There is no evidence from the surface of Venus that it once had a magnetic field but this does not rule out the possibility of an ancient dynamo because any record of remnant magnetism on the surface would likely have been erased during the global resurfacing event $300 - 500$ Ma (Schaber et al., 1992). In this section we describe how dynamo action was affected in an ancient terrestrial core when radioactive heating in the mantle was more important than today.

If we assume that all terrestrial dynamos are driven by convection, then the presence or absence of dynamo action in a terrestrial planet is directly controlled by the rate of heat transfer out of its core. Two fundamental conditions for maintaining a large core heat flow are (1) that the planet has a large surface heat flow in order to promote sub-solidus mantle convection that penetrates to the core, and (2) that radioactive heat production in the mantle not be so large that mantle convection cannot extract the necessary heat from the core. We note that a large core heat flow over long time-scales may lead to a faster crystallization of the core, which may add gravitational energy to the dynamo in the short run, but may ultimately lead to complete core crystallization. Therefore we consider a slightly super-adiabatic core heat flow to be sufficiently large to generate a strong magnetic field.

In the formalism of the optimal model developed in this study, a large surface heat flow results because we assume mobile lid whole-mantle convection. This condition allows the upper mantle thermal boundary layer to reach the planetary surface and the local Rayleigh number to remain close to the critical value for the onset of convection. In general, the Rayleigh number in the boundary layer and heat flow across the boundary layer are inversely

proportional for a constant ΔT, therefore the smaller the boundary layer Ra the larger the heat flow. On the other hand, stagnant lid mantle convection would introduce an additional, near surface layer on top of the convective boundary layer through which the heat flow must be transported by conduction because of the low or vanishing velocity there. This scenario may describe the present state of mantle convection on Venus and Mars. It has been proposed that ancient dynamos in Venus and Mars were maintained because those planets were subject to mobile lid mantle convection in the past, but that dynamo action in the core and mobile lid surface tectonics may have ended at around the same time (Nimmo, 2002; Stevenson, 2001). The presence of large amounts of water in the Earth's lithosphere has been proposed as a key ingredient in the maintenance of plate tectonics (Bercovici, 1998, 2003) and, therefore, indirectly maintaining the geodynamo over billions of years and could account for the longevity of Earth's magnetic field compared to Mars.

Radioactive heating in the mantles of the terrestrial planets was proportionately higher earlier on in their history, so in order to maintain core convection at this time a large amount of heat must be conducted through the surface. For example, the rate of heat produced by the decay of ^{238}U to ^{206}Pb (half life of 4.4 Gyr) was twice as high in the early solar system than it is today (Korenaga, 2006). Therefore, to prevent a net heating of the planet the surface temperature profile must adjust so that the total surface heat flow increases by the same amount. Generally the total heat budget for the mantle

$$Q_1 = Q_R + Q_{sec} + Q_c \tag{34}$$

includes secular cooling of the planet Q_{sec}. Let us consider a near-optimal planet like the Earth where the surface heat flow is near its optimal value and the core heat flow is super-adiabatic so that both Q_1 and Q_c are roughly constant over billions of years. Since the radioactive heat flow evolves as $Q_R \propto e^{-\lambda t}$, secular cooling must make up the difference so that $Q_{sec} \propto 1 - e^{-\lambda t}$. In the Earth, a slow increase in Q_{sec} will cool the initially hot core over

time and offers an explanation of the rather late onset of inner core solidification $1-2$ Ga (e.g. Labrosse et al., 2001; Davies, 2007).

In sub-optimal planets like Venus and Mars, Q_1 may initially be near optimal but this is not sustained over long periods of time. For such planets, it seems possible that if the optimal surface heat flow is less than Q_R then the near-surface dynamics of these planets may never have allowed for a significant amount of secular cooling or super-adiabatic core heat flow. In this case we take Q_{sec} and Q_c to be constant (or zero) so we can estimate the amount of melting that would occur in the surface boundary layer due to radioactivity. Assuming constant viscosity and $Ra = Ra_{crit}$ we write the total surface heat flow as a function of ΔT using (18) in (19),

$$Q_1 = \frac{2}{\sqrt{\pi}} A_1 k_1 \left(\frac{\beta}{Ra_{crit}} \right)^{1/3} (\Delta T_1)^{4/3} \tag{35}$$

where $\beta = \alpha g / \nu\kappa$. If radioactive heat generation exceeds the optimal surface heat flow by a factor ϵ so that $Q_R = \epsilon Q_1$ then (35) predicts an increase in ΔT_1 by a factor of $\epsilon^{3/4}$. Because any temperature jump larger than the critical ΔT_1 will bring the temperature profile above the silicate melting curve this will certainly lead to large scale melting of the boundary layer. For example, if $\epsilon = 2$ then ΔT_1 will increase by a factor of 1.68. Melting of the surface may be transient because heat is quickly radiated to space or may linger on time-scales comparable to the radioactive half-life. However, this is likely an upper estimate on the amount of melting because a hotter boundary layer will have a lower viscosity, a thinner boundary layer thickness, and a larger heat flow.

For a strong dynamo, radioactive heat production cannot be too large in the bulk of the mantle because as mentioned above the amount of heat that can be conducted across the upper thermal boundary layer for a sustained length of time is limited, even in a near-optimal, mobile lid planet like the Earth. If the heat produced by large amounts of radioactivity in the mantle swamps or exceeds the optimal limit set by the surface thermal boundary layer, then the mantle temperature will increase, which will decrease the temperature jump at

the CMB and with it the core heat flow. Indeed planets with very large amounts of mantle radioactivity and a low surface heat flow may have mantles so hot that the temperature gradient at the CMB is reversed and heat is conducted into the core, which would stably stratify the liquid core and suppress convection there. Whether this situation occurred in any terrestrial planet is conjectural because the positive feedback between temperature and viscosity may decrease the thermal boundary layer thickness enough to prevent this effect.

8 Summary and conclusions

In this study we define an optimal whole planet thermal state that maximizes thermal convection in the core and found the corresponding optimal dynamo magnetic field. This model assumes that the local Rayleigh number is critical for convection in the upper mantle thermal boundary layer, that the temperature profile is at the solidus in the boundary layers, and that heat transfer between the core and mantle is in equilibrium. We apply this optimal state to internal structure models for $1 - 10$ M_E terrestrial planets with a 32% or 65% core mass fraction.

We find that $1 - 10$ M_E terrestrial planets in the optimal state can produce surface magnetic fields that are $2 - 5$ times stronger than the geomagnetic field, and magnetic dipole moments $2 - 23$ times the geomagnetic dipole moment. Since these models have been constructed to be optimal for magnetic field generation, they likely represent an upper limit on the magnetic field intensities of a thermally driven dynamo. However, additional energy sources that may increase the energy flux available to drive the dynamo, such as tidal heating, gravitational energy released at a solid-liquid boundary, or core radioactivity, may act to increase the magnetic field strength further.

Planetary magnetic fields emit cyclotron radiation due to the interaction with energetic stellar wind electrons. Cyclotron radio emission from nearby magnetic exoplanets may be detectable in the near future, although the normal emission frequency from terrestrial-

type magnetic fields is likely below the Earth's ionospheric cutoff frequency. In general, the stronger the magnetic field the more intense the emission so the most promising targets would be those in an optimal dynamo conguration with a combination of driving sources and dynamics that maximize the magnetic field intensity. To this end, quantitative predictions of exoplanet magnetic field intensities can guide observers to the most promising targets. Also, cyclotron emission intensity increases with stellar wind intensity, while modulations of the emission may be caused by a highly eccentric orbit or interactions with other nearby magnetic planets, which could enhance the chances of detection.

References

Acuna, M., Connerney, J., Wasilewski, P., Lin, R., Anderson, K., Carlson, C., McFadden, J., Curtis, D., Mitchell, D., Reme, H., et al., 1998. Magnetic field and plasma observations at Mars: Initial results of the Mars Global Surveyor mission. Science 279 (5357), 1676.

Alfe, D., Gillan, M., Price, G., 2003. A Thermodynamics from first principles: temperature and composition of the Earth's core. Mineralogical Magazine 67 (1), 113–123.

Anderson, B., Acuna, M., Korth, H., Purucker, M., Johnson, C., Slavin, J., Solomon, S., McNutt Jr, R., 2008. The structure of Mercury's magnetic field from MESSENGER's first flyby. Science 321 (5885), 82.

Anderson, J., Schubert, G., 2007. Saturn's gravitational field, internal rotation, and interior structure. Science 317 (5843), 1384.

Bercovici, D., 1998. Generation of plate tectonics from lithosphere–mantle flow and void–volatile self-lubrication. Earth and Planetary Science Letters 154 (1-4), 139–151.

Bercovici, D., 2003. The generation of plate tectonics from mantle convection. Earth Planet. Sci. Lett. 205 (3-4), 107–121.

Boehler, R., 2007. Properties of Rocks and Minerals - High-Pressure Melting. In: Treatise on Geophysics. Vol. 2. Elsevier, Amsterdam, Ch. 18.

Boehler, R., Bargen, V., Chopelas, A., 1990. Melting, thermal expansion, and phase transitions of iron at high pressures. Journal of Geophysical Research 95, 21731–21736.

Butler, R., Wright, J., Marcy, G., Fischer, D., Vogt, S., Tinney, C., Jones, H., Carter, B., Johnson, J., McCarthy, C., et al., 2006. Catalog of Nearby Exoplanets 1. The Astrophysical Journal 646 (1), 505–522.

Chopelas, A., Boehler, R., 1992. Thermal expansivity in the lower mantle. Geophysical Research Letters 19 (19), 1983–1986.

Christensen, U., 2006. A deep dynamo generating Mercury's magnetic field. Nature 444 (7122), 1056–1058.

Christensen, U., Aubert, J., 2006. Scaling properties of convection-driven dynamos in rotating spherical shells and application to planetary magnetic fields. Geophys. J. Int. 166 (1), 97–114.

Christensen, U., Holzwarth, V., Reiners, A., 2009. Energy flux determines magnetic field strength of planets and stars. Nature 457, 167–169.

Christensen, U., Tilgner, A., 2004. Power requirement of the geodynamo from ohmic losses in numerical and laboratory dynamos. Nature 429 (6988), 169–171.

Christensen, U. R., Schmitt, D., Rempel, M., 2008. Planetary dynamos from a solar perspective. Space Science Reviews DOI 10.1007/s11214-008-9449-6.

Davies, G. F., 2007. Thermal Evolution of the Mantle. Vol. 9 of Treatise on Geophysics. Elsevier, Amsterdam, Ch. 8.

Dehant, V., Lammer, H., Kulikov, Y., Grießmeier, J., Breuer, D., Verhoeven, O., Karatekin, Ö., Van Hoolst, T., Korablev, O., Lognonné, P., 2007. Planetary Magnetic Dynamo Effect on Atmospheric Protection of Early Earth and Mars. Space Science Reviews 129 (1), 279–300.

Desch, M., Kaiser, M., 1984. Predictions for Uranus from a radiometric Bode's law. Nature 310, 755–757.

Dziewonski, A., Anderson, D., 1981. Preliminary reference Earth model. Phys. Earth Planet. Inter. 25 (4).

Elsasser, W., 1946. Induction Effects in Terrestrial Magnetism Part II. The Secular Variation. Physical Review 70 (3-4), 202–212.

Farrell, W., Desch, M., Zarka, P., 1999. On the possibility of coherent cyclotron emission from extrasolar planets. J. Geophys. Res. 104 (E6).

Farrell, W., Lazio, T., Zarka, P., Bastian, T., Desch, M., Ryabov, B., 2004. The radio search for extrasolar planets with LOFAR. Planetary and Space Science 52 (15), 1469–1478.

Fischer, D., 2008. Mapping the realm of hot Jupiters. Physica Scripta 130, 014002.

Griessmeier, J., Stadelmann, A., Penz, T., Lammer, H., Selsis, F., Ribas, I., Guinan, E., Motschmann, U., Biernat, H., Weiss, W., 2004. The effect of tidal locking on the magnetospheric and atmospheric evolution of "Hot Jupiters". Astronomy and Astrophysics 425 (2), 753–762.

Gubbins, D., Alfe, D., Masters, G., Price, G., Gillan, M., 2004. Gross thermodynamics of two-component core convection. Geophys. J. Int. 157 (3), 1407–1414.

Guillot, T., Jan. 2005. The Interiors of Giant Planets: Models and Outstanding Questions. Annual Review of Earth and Planetary Sciences 33, 493–530.

Gurnett, D., Persoon, A., Kurth, W., Groene, J., Averkamp, T., Dougherty, M., Southwood, D., 2007. The variable rotation period of the inner region of Saturn's plasma disk. Science 316 (5823), 442.

Hernlund, J. W., Labrosse, S., 2007. Geophysically consistent values of the perovskite to post-perovskite transition Clapeyron slope. Geophys. Res. Lett. 34.

Hirschmann, M., 2000. Mantle solidus: experimental constraints and the effects of peridotite composition. Geochemistry Geophysics Geosystems 1 (10), 1042.

Hirth, G., Kohlstedt, D., 1996. Water in the oceanic upper mantle: implications for rheology, melt extraction and the evolution of the lithosphere. Earth and Planetary Science Letters 144 (1-2), 93–108.

Hofmeister, A., 1999. Mantle values of thermal conductivity and the geotherm from phonon lifetimes. Science 283 (5408), 1699.

Holland, K., Ahrens, T., 1997. Melting of (Mg, Fe) 2SiO4 at the core-mantle boundary of the Earth. Science 275 (5306), 1623.

Ida, S., Lin, D., 2004. Toward a Deterministic Model of Planetary Formation. I. A Desert in the Mass and Semimajor Axis Distributions of Extrasolar Planets. The Astrophysical Journal 604 (1), 388–413.

Ito, E., Takahashi, E., 1989. Postspinel transformations in the system Mg 2 SiO 4-Fe 2 SiO 4 and some geophysical implications. J. geophys. Res 94 (10,637).

Jaupart, C., Labrosse, S., Mareschal, J. C., 2007. Temperatures, heat and energy in the mantle of the Earth. Vol. 7 Mantle Dynamics of Treatise on Geophysics. Elsevier, Amsterdam, Ch. 2, pp. 253–305.

Jones, C. A., 2007. Thermal and compositional convection in the outer core. Vol. 8 of Treatise on Geophysics. Elsevier, Amsterdam, pp. 131–185.

Karato, S., Jung, H., 1998. Water, partial melting and the origin of the seismic low velocity and high attenuation zone in the upper mantle. Earth and Planetary Science Letters 157 (3-4), 193–207.

Kassim, N., Lazio, T., Ray, P., Crane, P., Hicks, B., Stewart, K., Cohen, A., Lane, W., 2004. The low-frequency array (LOFAR): opening a new window on the universe. Planetary and Space Science 52 (15), 1343–1349.

Kasting, J., 1995. O2 concentrations in dense primitive atmospheres: commentary. Planetary and Space Science 43 (1-2), 11–13.

Kohlstedt, D., 2007. Properties of rocks and minerals—Constitutive equations, rheological behavior, and viscosity of rocks. Treatise on Geophysics 2, 389–417.

Korenaga, J., 2006. Archean geodynamics and the thermal evolution of Earth. Geophysical Monograph-American Geophysical Union 164, 7.

Labrosse, S., Jaupart, C., 2007. Thermal evolution of the Earth: Secular changes and fluctuations of plate characteristics. Earth and Planetary Science Letters 260 (3-4), 465–481.

Labrosse, S., Poirier, J., Le Mouël, J., 2001. The age of the inner core. Earth Planet. Sci. Lett. 190 (3-4), 111–123.

Lammer, H., Kasting, J., Chassefière, E., Johnson, R., Kulikov, Y., Tian, F., 08 2008. Atmospheric Escape and Evolution of Terrestrial Planets and Satellites. Space Science Reviews 139 (1), 399–436.

Lammer, H., Lichtenegger, H., Kulikov, Y., Grießmeier, J., Terada, N., Erkaev, N., Biernat, H., Khodachenko, M., Ribas, I., Penz, T., et al., 2007. Coronal mass ejection (CME) activity of low mass M stars as an important factor for the habitability of terrestrial exoplanets. II. CME-induced ion pick up of Earth-like exoplanets in close-in habitable zones. Astrobiology 7 (1), 185–207.

Laughlin, G., Bodenheimer, P., Adams, F., 2004. The core accretion model predicts few Jovian-mass planets orbiting red dwarfs. The Astrophysical Journal Letters 612 (1), 73–76.

Lay, T., Hernlund, J., Garnero, E., Thorne, M., 2006. A post-perovskite lens and D"heat flux beneath the central Pacific. science 314 (5803), 1272.

Lazio, T., Carmichael, S., Clark, J., Elkins, E., Gudmundsen, P., Mott, Z., Szwajkowski, M., Hennig, L., 2010. Planetary Magnetospheric Emission Survey. The Astronomical Journal 139, 96–101.

Lecacheux, A., 1991. On the feasibility of extra-solar planetary detection at very low radio frequencies. Proceedings of Bioastronomy, the search for extraterrestrial life J. Heidmann and M. Klein Eds.(Springer).

Lin, J., Campbell, A., Heinz, D., Shen, G., 2003. Static compression of iron-silicon alloys: Implications for silicon in the Earth's core. J. Geophys. Res 108 (B1), 11–1.

Mosenfelder, J., Asimow, P., Ahrens, T., 2007. Thermodynamic properties of Mg2SiO4 liquid at ultra-high pressures from shock measurements to 200 GPa on forsterite and wadsleyite. J. Geophys. Res 112.

Nimmo, F., 2002. Why does Venus lack a magnetic field? Geology 30 (11), 987–990.

Nimmo, F., 2007. Thermal and compositional evolution of the core. Vol. 9 of Treatise on Geophysics. Elsevier, Amsterdam, Ch. 9, Evolution of Earth, Ed: Stevenson, D., pp. 217–241.

Nimmo, F., Stevenson, D., 2000. Influence of early plate tectonics on the thermal evolution and magnetic field of Mars. Journal of geophysical research 105 (E5), 11969–11980.

Oganov, A., 2007. Theory and Practice - Thermodynamics, Equations of State, Elasticity, and Phase Transitions of Minerals at High Pressures and Temperatures. In: Schubert, G. (Ed.), Treatise on Geophysics. Elsevier, Amsterdam, pp. 121 – 152.

Olson, P., Christensen, U., 2006. Dipole moment scaling for convection-driven planetary dynamos. Earth Planet. Sci. Lett. 250 (3-4), 561–571.

Olson, P., Driscoll, P., Amit, H., 2009. Dipole collapse and reversal precursors in a numerical dynamo. Phys. Earth Planet. Inter. 173, 121–140.

O'Neill, C., Jellinek, A. M., Lenardic, A., 9 2007. Conditions for the onset of plate tectonics on terrestrial planets and moons. Earth and Planetary Science Letters 261 (1-2), 20–32.

Poirier, J., 1991. Introduction to the Physics of the Earth's Interior. Cambridge University Press.

Roberts, P. H., 2007. Theory of the geodynamo. Vol. 8 of Treatise on Geophysics. Elsevier, Amsterdam, Ch. 3.

Roberts, P. H., Jones, C. A., Calderwood, A. R., 2003. Earth's core and lower mantle. Earth's Core and Lower Mantle. Taylor & Francis, Ch. 5 Energy fluxes and ohmic dissipation in the earth's core, pp. 100–129.

Sanchez-Lavega, A., 2004. The magnetic field in giant extrasolar planets. The Astrophysical Journal 609 (2), 87–90.

Schaber, G., Strom, R., Moore, H., Soderblom, L., Kirk, R., Chadwick, D., Dawson, D., Gaddis, L., Boyce, J., Russell, J., 1992. Geology and distribution of impact craters on Venus: What are they telling us? Journal of Geophysical Research-Planets 97 (E8).

Schneider, J., 2010. The Extrasolar Planets Encyclopedia. www.exoplanet.eu.

Schubert, G., Cassen, P., Young, R., 1979. Core cooling by subsolidus mantle convection. In: (Topical Conference on Origins of Planetary Magnetism, Houston, Tex., Nov. 8-11, 1978.) Physics of the Earth and Planetary Interiors. Vol. 20.

Schubert, G., Turcotte, D., Olson, P., 2001. Mantle Convection in the Earth and Planets. Cambridge Univ. Press, New York.

Seager, S., Kuchner, M., Hier-Majumder, C., Militzer, B., 2007. Mass-radius relationships for solid exoplanets. The Astrophysical Journal 669 (2), 1279–1297.

Shim, S., 2008. The postperovskite transition. Annu. Rev. Earth Planet. Sci. 36, 569–99.

Shkolnik, E., Bohlender, D., Walker, G., Collier Cameron, A., 2008. The On/Off Nature of Star-Planet Interactions 1. The Astrophysical Journal 676 (1), 628–638.

Shkolnik, E., Walker, G., Bohlender, D., 2003. Evidence for Planet-induced Chromospheric Activity on HD 179949. The Astrophysical Journal 597 (2), 1092–1096.

Sotin, C., Grasset, O., Mocquet, A., 2007. Mass–radius curve for extrasolar Earth-like planets and ocean planets. Icarus 191 (1), 337–351.

Stacey, F., 1992. Physics of the Earth. Brisbane, Australia: Brookfield Press.

Stacey, F., Davis, P., 2004. High pressure equations of state with applications to the lower mantle and core. Physics of the Earth and Planetary Interiors 142 (3-4), 137–184.

Stacey, F., Loper, D., 2007. A revised estimate of the conductivity of iron alloy at high pressure and implications for the core energy balance. Phys. Earth Planet. Inter. 161 (1-2), 13–18.

Stevenson, D., 2001. Mars' core and magnetism. Nature 412 (6843), 214–219.

Stevenson, D., 2003. Planetary magnetic fields. Earth Planet. Sci. Lett. 208 (1-2), 1–11.

Stixrude, L., Lithgow-Bertelloni, C., 2005. Thermodynamics of mantle minerals-I. Physical properties. Geophysical Journal International 162 (2), 610–632.

Turcotte, D., Schubert, G., 2002. Geodynamics. Cambridge University Press.

Uchida, T., Wang, Y., Rivers, M., Sutton, S., 2001. Stability field and thermal equation of state of e-iron determined by synchrotron X-ray diffraction in a multianvil apparatus. J. Geophys. Res 106 (B10), 21799–21810.

Valencia, D., O'Connell, R., Sasselov, D., 2006. Internal structure of massive terrestrial planets. Icarus 181 (2), 545–554.

Valencia, D., O'Connell, R., Sasselov, D., 2007. Inevitability of Plate Tectonics on Super-Earths. The Astrophysical Journal Letters 670 (1), 45–48.

Van den Berg, A., Yuen, D., Allwardt, J., 2002. Non-linear effects from variable thermal conductivity and mantle internal heating: implications for massive melting and secular cooling of the mantle. Physics of the Earth and Planetary Interiors 129 (3), 359–376.

Van der Hilst, R., de Hoop, M., Wang, P., Shim, S., Ma, P., Tenorio, L., 2007. Seismostratigraphy and thermal structure of Earth's core-mantle boundary region. science 315 (5820), 1813.

Vinet, P., Rose, J., Ferrante, J., Smith, J., 1989. Universal features of the equation of state of solids. Journal of Physics: Condensed Matter 1, 1941–1963.

Weast, R., 2009. Handbook of Chemistry and Physics, 89th edition.
URL `http://www.hbcpnetbase.com/`

Yantis, W., Sullivan III, W., Erickson, W., 1977. A Search for Extra-Solar Jovian Planets by Radio Techniques. In: Bulletin of the American Astronomical Society. Vol. 9. p. 453.

Zapolsky, H., Salpeter, E., 1969. The mass-radius relation for cold spheres of low mass. The Astrophysical Journal 158, 809.

Zarka, P., 2007. Plasma interactions of exoplanets with their parent star and associated radio emissions. Planetary and Space Science 55 (5), 598–617.

Zarka, P., Treumann, R., Ryabov, B., Ryabov, V., 2001. Magnetically-driven planetary radio emissions and application to extrasolar planets. Astrophysics and Space Science 277 (1), 293–300.

Zerr, A., Diegeler, A., Boehler, R., 1998. Solidus of Earth's deep mantle. Science 281 (5374), 243.

Parameter	Peridotite	Perovskite	Post-Perovskite	Liquid Fe	Solid Fe
ρ_0 (kg m^{-3})	3226	4000	4100	6900	7300
K_0 (GPa)	128	200	231	125	165
K_0' (n.d.)	4.2	4.0	4.0	5.5	4.9
γ_0 (n.d.)	0.99	1.0	1.5	1.60	1.60
γ_1 (n.d.)	2.1	1.4	1.4	0.92	0.92
α_0 ($\times 10^{-6}$ K^{-1})	20	20	20	40	40

Table 1
Material constants of each layer. Constants for peridotite (olivine) and perovskite are similar to those of Stixrude and Lithgow-Bertelloni (2005). Constants for post-perovskite are similar to those of Shim (2008). Constants for liquid and solid Fe are similar to those of Stacey and Davis (2004), Lin et al. (2003), Uchida et al. (2001), and Boehler et al. (1990). Non-dimensional quantities are denoted (n.d.).

Fig. 1. Temperature profile for the present-day Earth model.

Fig. 2. Radial structure profiles for $1 - 10$ M_E optimal models and the Earth model (labeled E). (a): Density profiles for 32% core mass fraction (CMF). (b): Density profiles for 65% CMF. (c): Pressure profiles for 32% CMF. (d): Pressure profiles for 65% CMF. Note that the Earth model density profile overlaps with the optimal 1 M_E model, except for the jump in the Earth model at the inner core boundary. The Earth model pressure profile is indistinguishable from the optimal 1 M_E model.

Fig. 3. Temperature profiles for $1 - 10 M_E$ optimal models and the Earth model (labeled E). (a): 32% core mass fraction (CMF). (b): 65% CMF

Fig. 4. Optimal thermal properties in the upper mantle boundary layer. Thermal boundary layer (a) thickness δ_1, (b) temperature jump ΔT_1, (c) surface heat flow Q_1, and (d) boundary layer Rayleigh number Ra_1.

Fig. 5. Optimal thermal properties in the lower mantle boundary layer. Thermal boundary layer (a) thickness δ_2, (b) temperature jump ΔT_2, (c) CMB heat flow Q_c, and (d) boundary layer Rayleigh number Ra_2.

Fig. 6. Mobile-lid surface properties. (a): Mean surface age τ. (b): Cell length λ. (c): Mean surface velocity u.

Fig. 7. Core convection and magnetic field properties. (a) Convective core heat flow Q_{conv}. (b) Magnetic moment μ. (c) CMB magnetic field intensity B_c. (d) Planetary surface magnetic field intensity B_s. Geomagnetic units: $\mu_\oplus = 78$ ZAm^2, $B_{c,\oplus} = 0.264$ mT, $B_{s,\oplus} = 30,300$ nT.

Fig. 8. Cyclotron radio emission spectrum for optimal 32% and 65% CMF exoplanets. Shaded region indicates the terrestrial dynamo region for cyclotron emission. Solid curves are the potential emission from $1-10$ M_E exoplanets orbiting at $a = 0.02$ AU around α Centauri at $s = 1.33$ pc and GJ876 at $s = 4.72$ pc from Earth. Also shown are the expected emissions for nearby exoplanets GJ674b, GJ581b, GJ581e, 55Cnc e, and HD7924b all assuming 65% CMF, and for Earth, Jupiter, and Saturn assuming they orbit α Centauri. The ionospheric cutoff at 10 MHz sets the lower frequency limit for ground-based radio telescopes such as LOFAR, shown for an 8 hour exposure detection threshold.

2) Figure 1

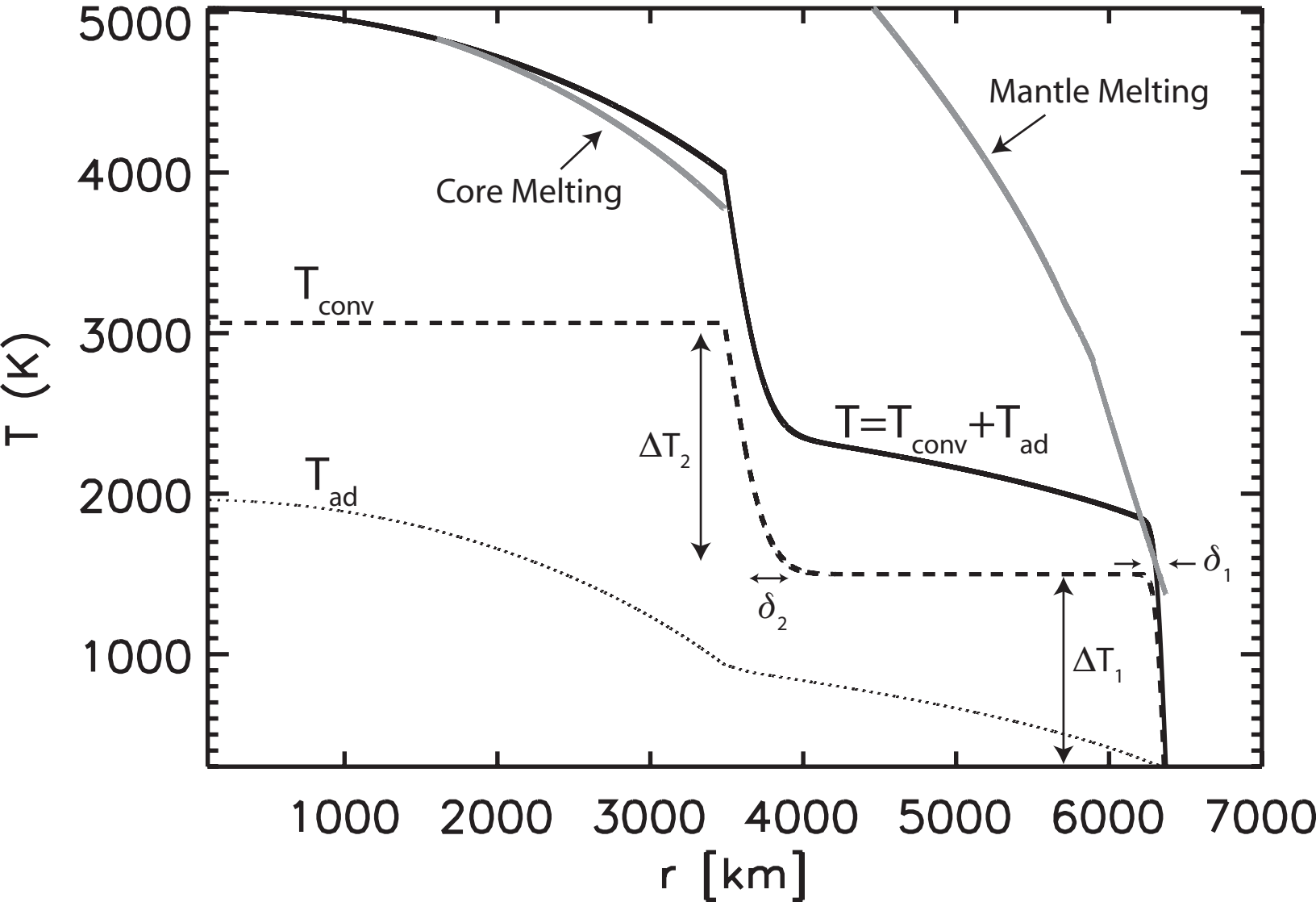
5000
4000
3000
2000
1000
T (K)
1000
2000
3000
4000
5000
6000
7000
r [km]
Core Melting
Mantle Melting
T_conv
T_ad
T=T_conv+T_ad
ΔT_2
ΔT_1
δ_2
δ_1

2) Figure 2

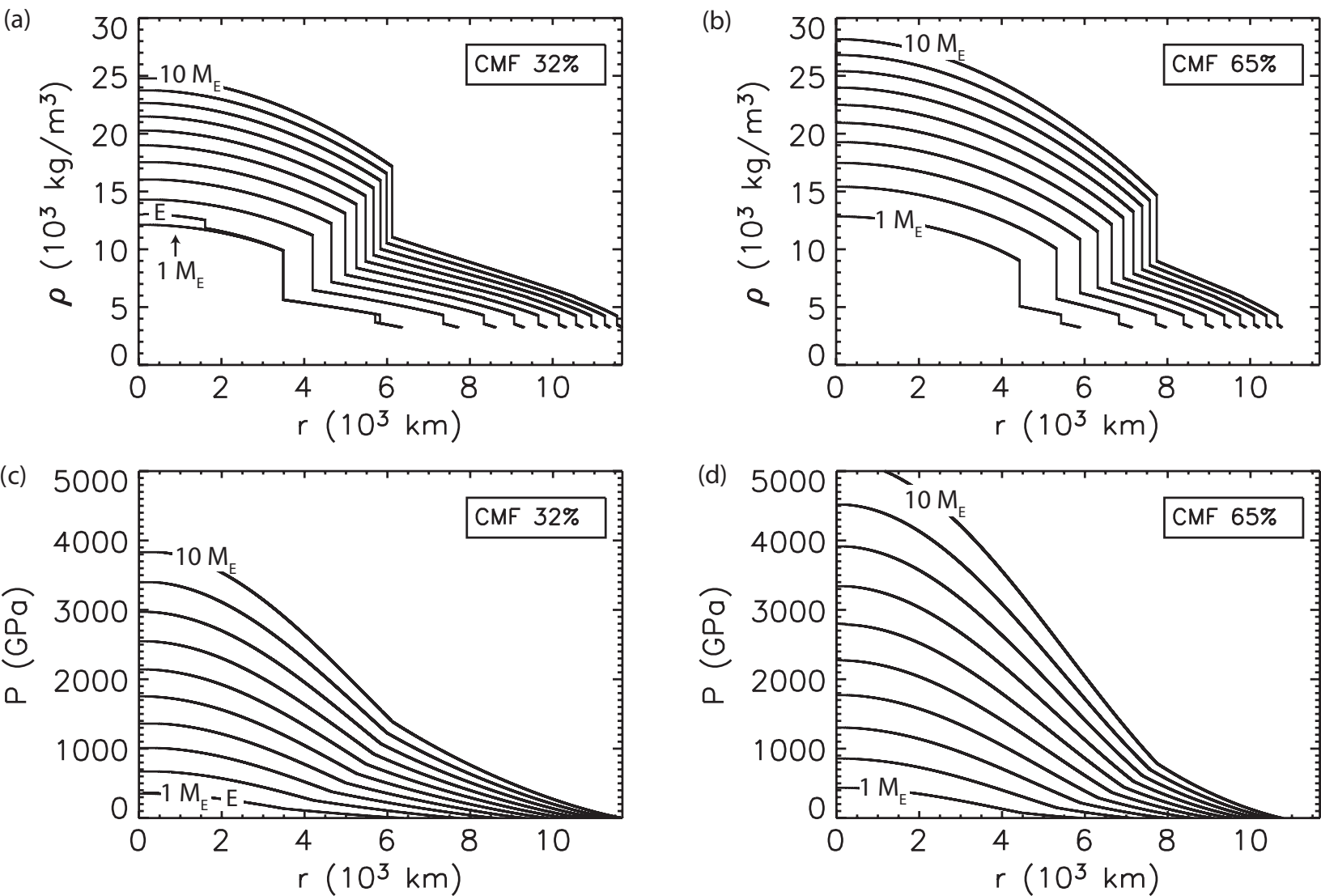
(a)
CMF 32%
10 M_E
E
1 M_E
ρ (10³ kg/m³)
r (10³ km)
(b)
CMF 65%
10 M_E
1 M_E
ρ (10³ kg/m³)
r (10³ km)
(c)
CMF 32%
10 M_E
1 M_E - E
P (GPa)
r (10³ km)
(d)
CMF 65%
10 M_E
1 M_E
P (GPa)
r (10³ km)

2) Figure 3

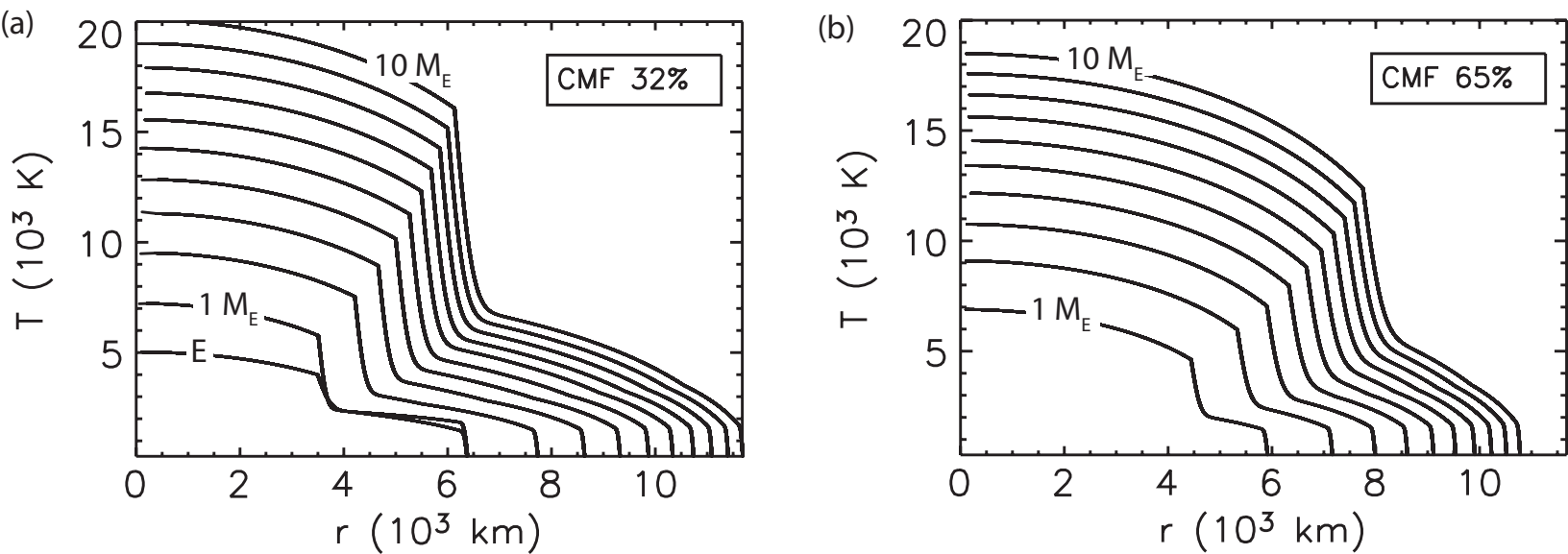
(a)
20
15
10
5
T (10³ K)
10 M_E
1 M_E
E
CMF 32%
0
2
4
6
8
10
r (10³ km)
(b)
20
15
10
5
T (10³ K)
10 M_E
1 M_E
CMF 65%
0
2
4
6
8
10
r (10³ km)

2) Figure 4

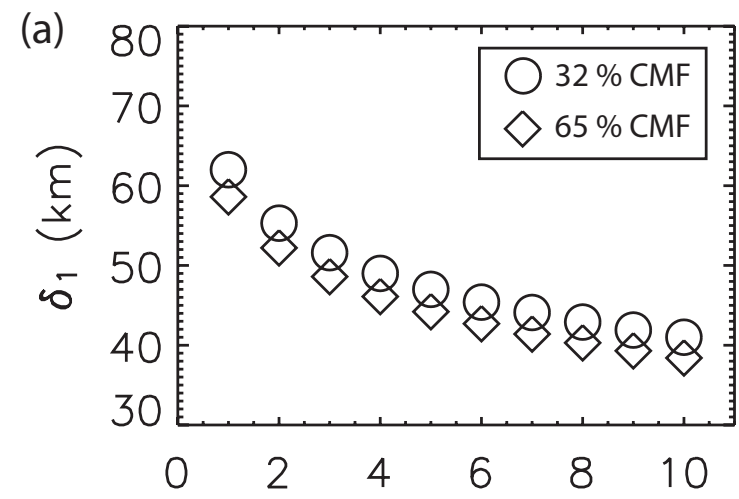
(a)
80
70
60
50
40
30
δ_1 (km)
32 % CMF
65 % CMF
0
2
4
6
8
10

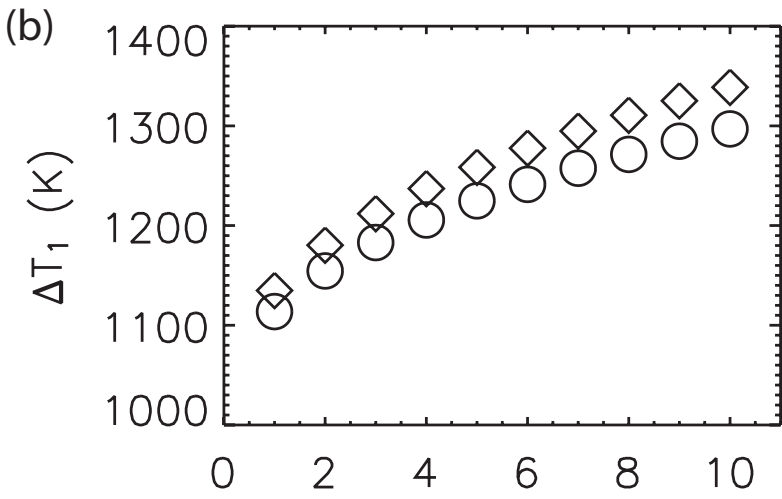
(b)
1400
1300
1200
1100
1000
ΔT_1 (K)
0
2
4
6
8
10

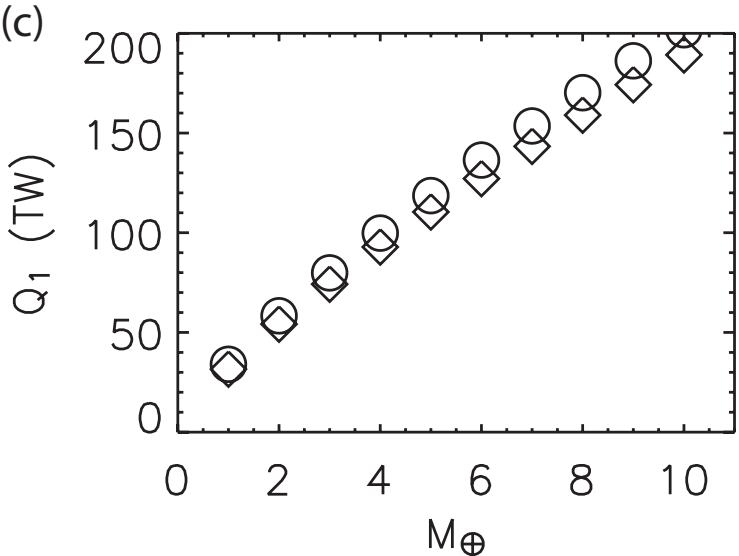
(c)
200
150
100
50
0
Q_1 (TW)
0
2
4
6
8
10
$M_\oplus$

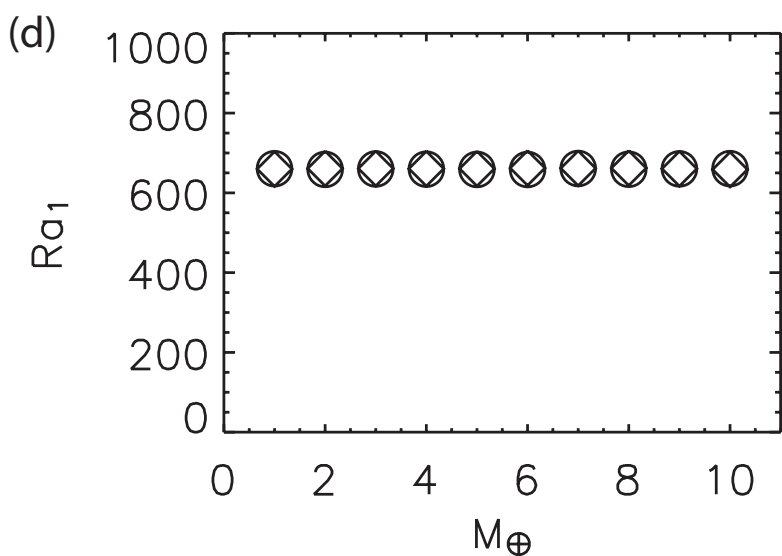
(d)
1000
800
600
400
200
0
Ra_1
0
2
4
6
8
10
$M_\oplus$

2) Figure 5

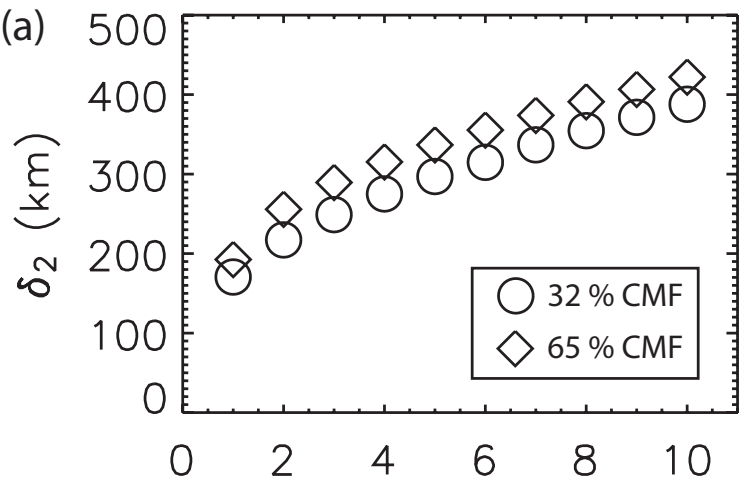
(a)
δ_2 (km)
500
400
300
200
100
0
0
2
4
6
8
10
32 % CMF
65 % CMF

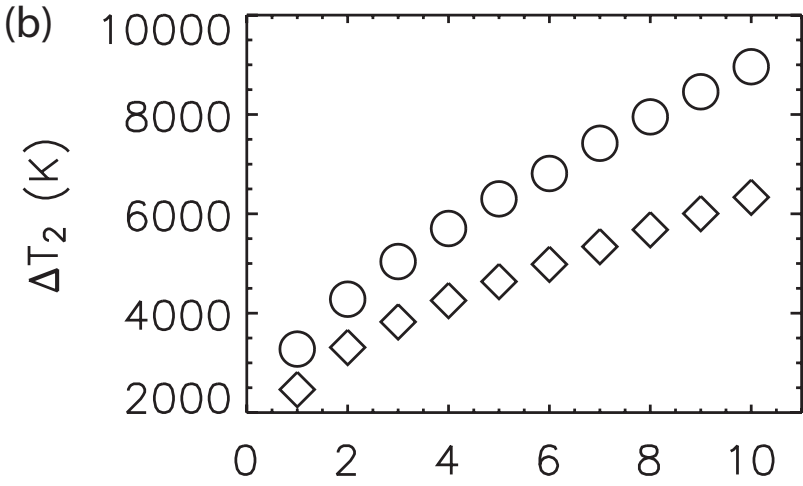
(b)
ΔT_2 (K)
10000
8000
6000
4000
2000
0
2
4
6
8
10

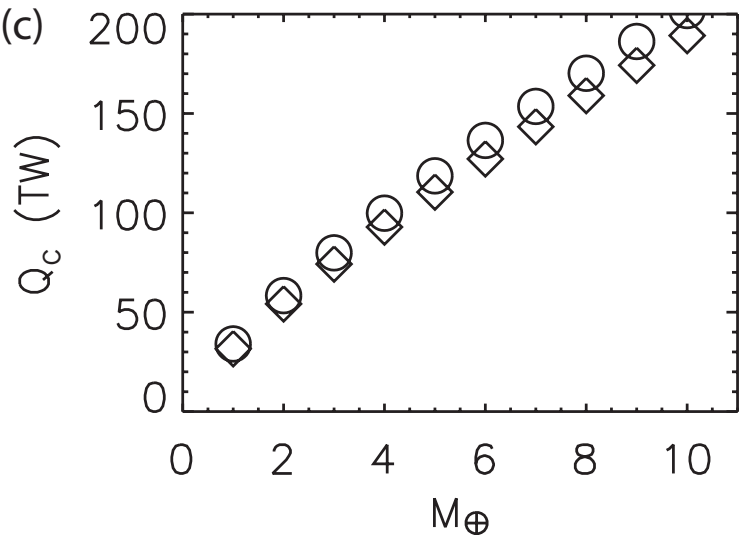
(c)
Q_c (TW)
200
150
100
50
0
0
2
4
6
8
10
$M_\oplus$

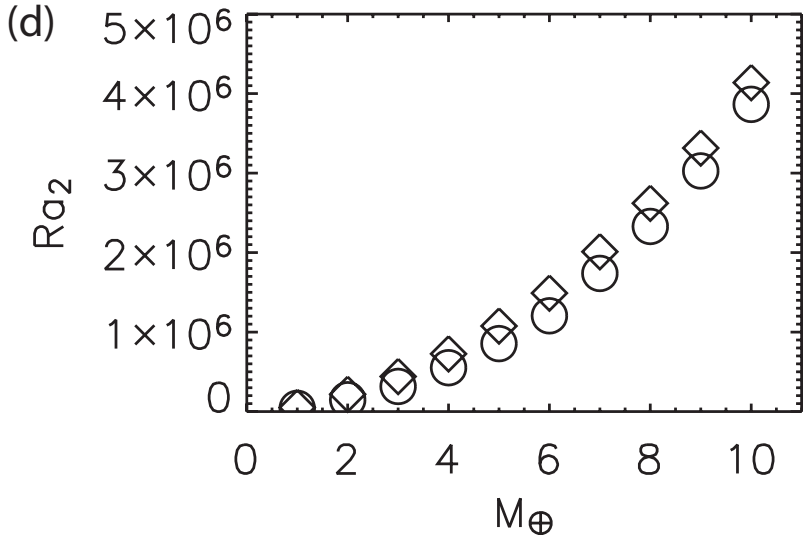
(d)
Ra_2
5×10^6
4×10^6
3×10^6
2×10^6
1×10^6
0
0
2
4
6
8
10
$M_\oplus$

2) Figure 6

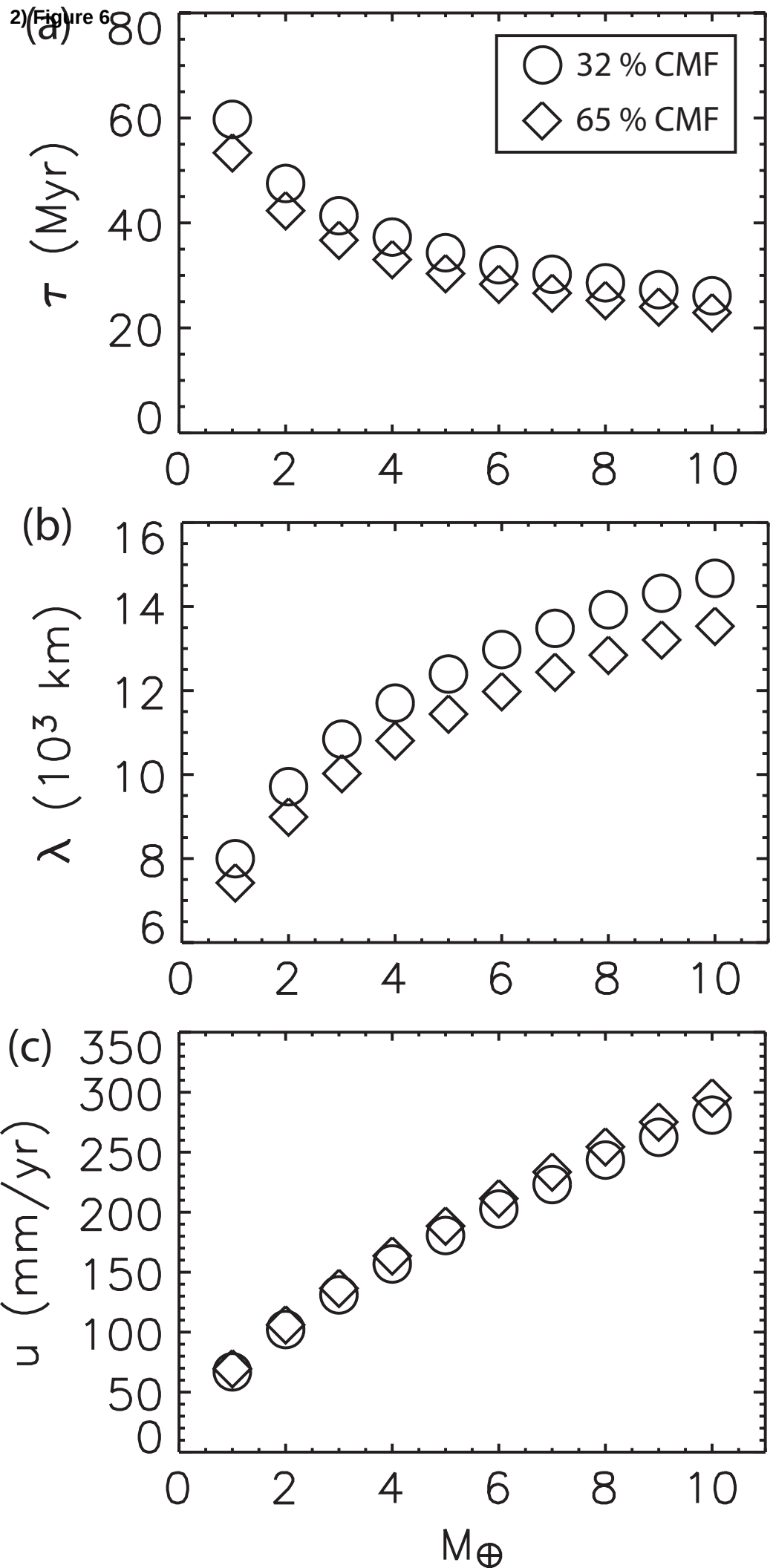
(a)
32 % CMF
65 % CMF
τ (Myr)
0
20
40
60
80
0
2
4
6
8
10
(b)
λ (10³ km)
6
8
10
12
14
16
0
2
4
6
8
10
(c)
u (mm/yr)
0
50
100
150
200
250
300
350
0
2
4
6
8
10
M⊕

2) Figure 7

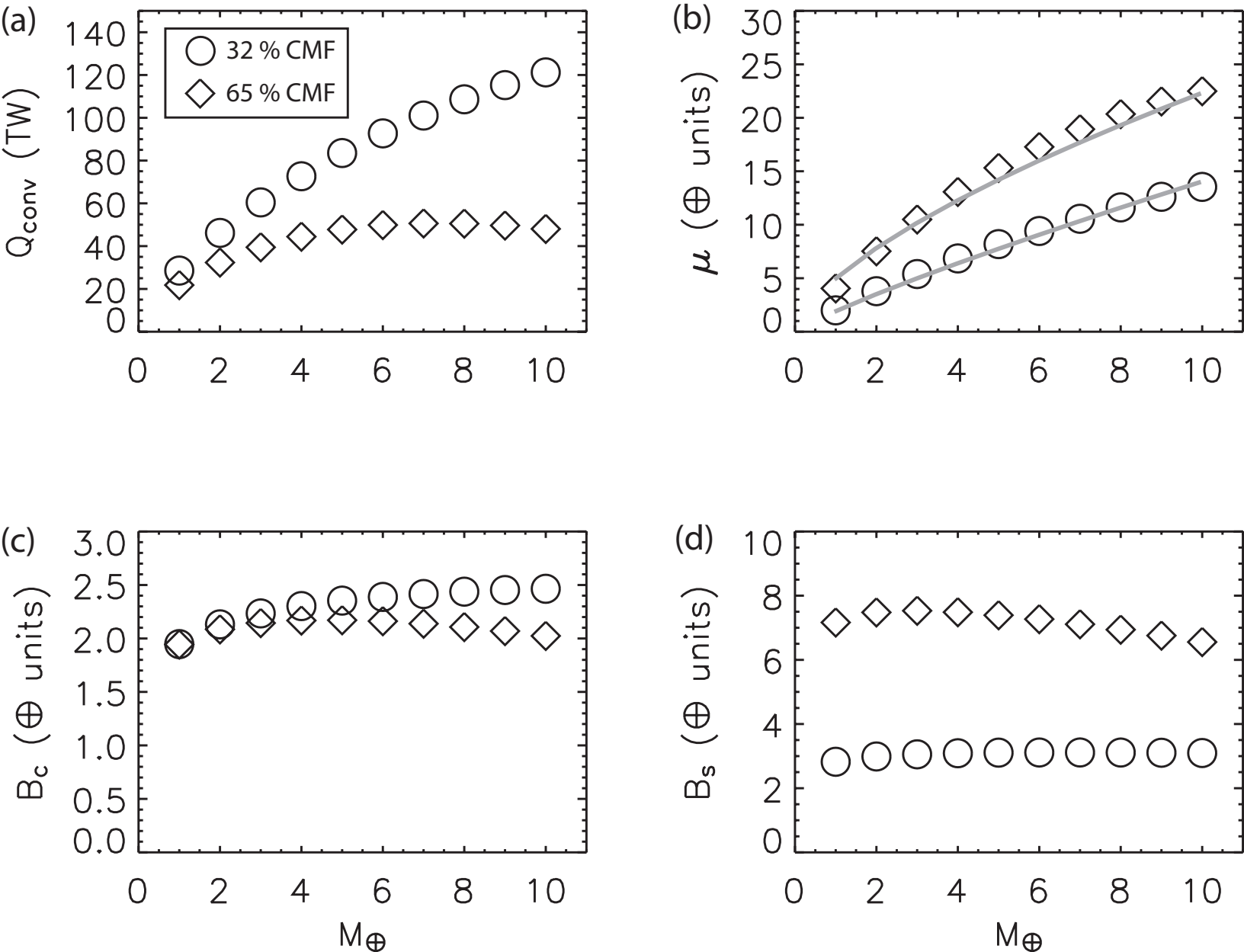
(a)
Q_{conv} (TW)
32 % CMF
65 % CMF
(b)
μ ($\oplus$ units)
(c)
B_c ($\oplus$ units)
$M_\oplus$
(d)
B_s ($\oplus$ units)
$M_\oplus$

2) Figure 8

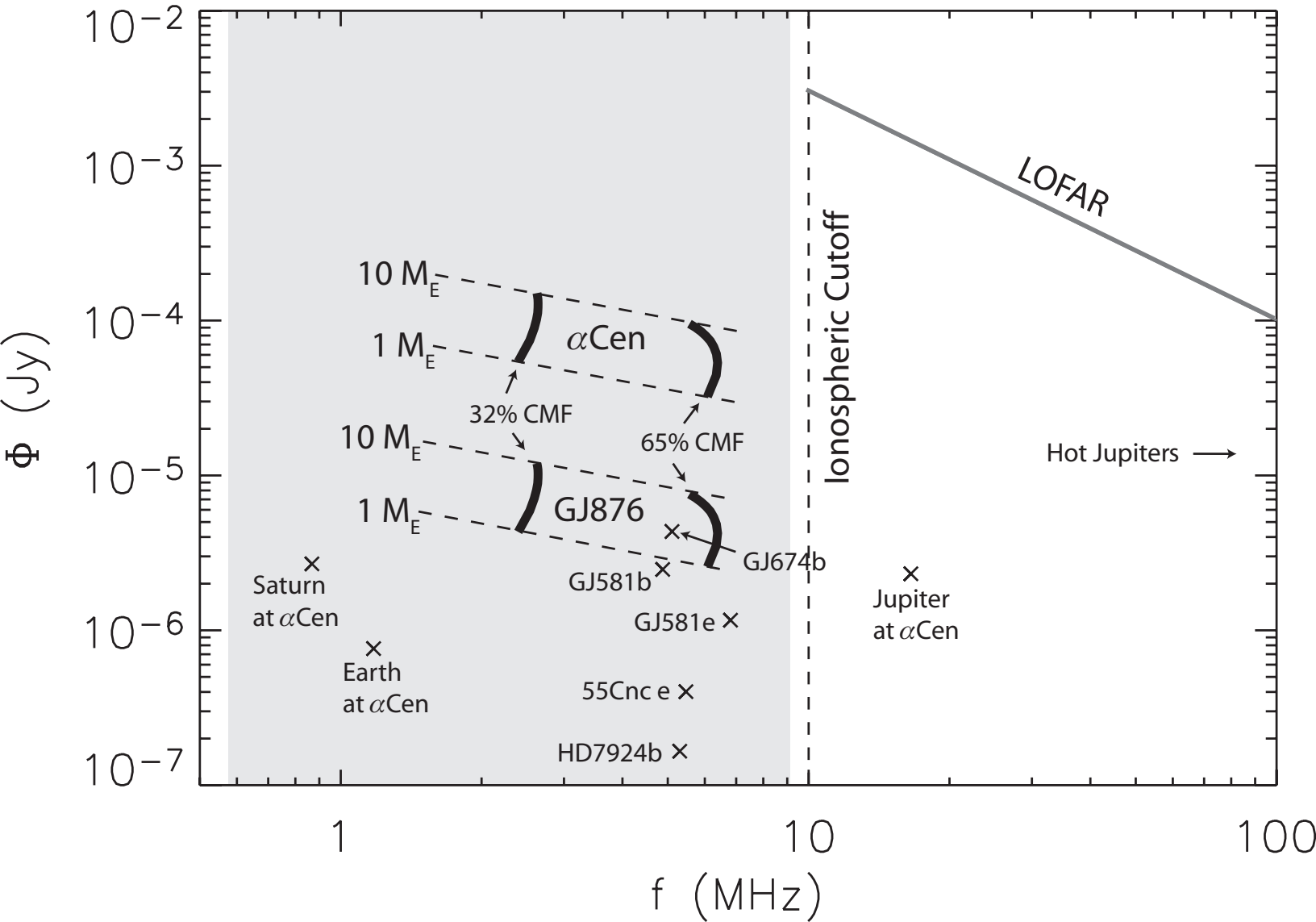
10 M_E
1 M_E
αCen
32% CMF
65% CMF
10 M_E
1 M_E
GJ876
GJ674b
GJ581b
GJ581e
55Cnc e
HD7924b
Saturn at αCen
Earth at αCen
Jupiter at αCen
Ionospheric Cutoff
LOFAR
Hot Jupiters
Φ (Jy)
f (MHz)
10^−2
10^−3
10^−4
10^−5
10^−6
10^−7
1
10
100